nature physics

Article

https://doi.org/10.1038/s41567-025-02922-9

Neutron scattering and thermodynamic evidence for emergent photons and fractionalization in a pyrochlore spin ice

Received: 15 November 2024

Accepted: 24 April 2025

Published online: 19 June 2025

Check for updates

Bin Gao[1,10], Félix Desrochers[2,10], David W. Tam[3,10], Diana M. Kirschbaum[4,10], Paul Steffens[5], Arno Hiess[5,6], Duy Ha Nguyen[4], Yixi Su[7], Sang-Wook Cheong[8], Silke Paschen[4] ✉, Yong Baek Kim[2] ✉ & Pengcheng Dai[1,9] ✉

The three-dimensional pyrochlore lattice of corner-sharing tetrahedra can host a quantum spin ice, a quantum analogue of the classical spin ice found in other pyrochlore compounds. This state can manifest a quantum spin liquid, and indeed, these compounds are predicted to have emergent gauge fields that produce linearly dispersing collective magnetic excitations near zero energy, in addition to the presence of higher-energy spinon excitations. Here we use polarized neutron scattering experiments on single crystals of the $Ce_2Zr_2O_7$ pyrochlore. We find evidence for magnetic excitations near zero energy, in addition to signatures of spinons at higher energies. Furthermore, we perform heat capacity measurements and find behaviour consistent with the cubic-in-temperature dependence expected for linearly dispersing gapless bosonic modes. Comparing the observed magnetic excitations with theoretical calculations, we argue that $Ce_2Zr_2O_7$ is a strong candidate for a dipolar–octupolar quantum spin ice with dominant dipolar Ising interactions.

Quantum spin liquids (QSLs) are phases of interacting quantum spins in a crystalline solid with long-range entangled ground states and no magnetic order down to zero temperature[1–5]. Although Anderson proposed their existence for a two-dimensional triangular lattice in 1973 (ref. 6), the conclusive identification of a QSL material and its associated microscopic Hamiltonian is still lacking[1–5], despite the relevance to high-transition-temperature superconductivity[7,8]. For the spin $S = 1/2$ two-dimensional honeycomb lattice, Kitaev's exactly solvable model with bond-dependent nearest-neighbour interactions has a QSL ground state, where the excitations are itinerant Majorana fermions and static Z_2 fluxes relevant for fault-tolerant quantum computation[9,10]. Despite intensive efforts, there is currently no conclusive identification of a Kitaev QSL material[11]. For $S = 1/2$ two-dimensional kagome and triangular lattice magnets, although there are many reports of fractionalized excitations consistent with a spinon Fermi surface QSL[12–19], the microscopic Hamiltonian is difficult to simulate[13,20,21].

In three-dimensional (3D) rare-earth pyrochlore magnets with a large effective moment, Ising-like spins decorating the corner-sharing tetrahedra (Fig. 1a) form a constrained paramagnet in which the system is energetically restricted to the degenerate 'two-in–two-out' classical spin ice (CSI) states, analogous to the 'two-near–two-far' rules of the covalent $2H^+–O^{2-}$ bonding distances in water ice[22,23]. This set of local

[1]Department of Physics and Astronomy, Rice University, Houston, TX, USA. [2]Department of Physics, University of Toronto, Toronto, Ontario, Canada. [3]PSI Center for Neutron and Muon Sciences, Paul Scherrer Institut, Villigen PSI, Switzerland. [4]Institute of Solid State Physics, Vienna University of Technology, Vienna, Austria. [5]Institut Laue-Langevin, Grenoble Cedex 9, France. [6]European Spallation Source ERIC, Lund, Sweden. [7]Jülich Centre for Neutron Science (JCNS) at Heinz Maier-Leibnitz Zentrum (MLZ), Forschungszentrum Jülich, Garching, Germany. [8]Keck Center for Quantum Magnetism and Department of Physics and Astronomy, Rutgers University, Piscataway, NJ, USA. [9]Smalley-Curl Institute, Rice University, Houston, TX, USA. [10]These authors contributed equally: Bin Gao, Félix Desrochers, David W. Tam, Diana M. Kirschbaum. ✉e-mail: paschen@ifp.tuwien.ac.at; yongbaek.kim@utoronto.ca; pdai@rice.edu

https://doi.org/10.1038/s41567-025-02922-9

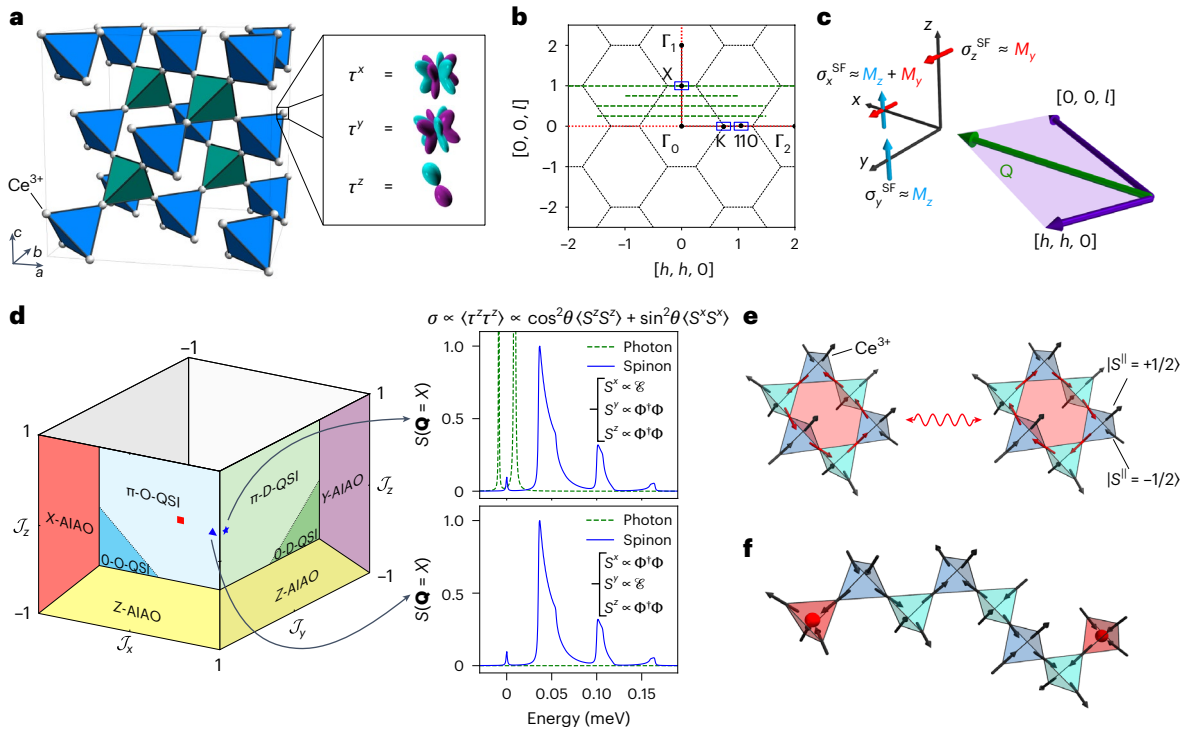

Fig. 1 | Summary of crystal structure, Brillouin zone, phase diagram, expected experimental signatures and excitations of $Ce_2Zr_2O_7$. **a**, Network of corner-sharing tetrahedra formed by the magnetic Ce^{3+} ions in $Ce_2Zr_2O_7$. The low-energy Kramers doublet of the Ce^{3+} ion can be modelled by the pseudospins-1/2 $\vec{\tau} = (\tau^x, \tau^y, \tau^z)$ that have octupolar and dipolar magnetic charge densities. **b**, (h, h, l) scattering plane. The dashed black lines mark the zone boundary; the blue boxes, the momentum transfer of the energy scans reported in Fig. 2; the green dashed lines, the momenta along which the elastic scans presented in Fig. 3 were measured; and the red dotted lines, the momentum cuts along which both elastic and inelastic scans presented in Figs. 3 and 4 were measured. **c**, Scattering geometry of polarized neutron scattering experiment in the (h, h, l) plane. Incident neutron beams are polarized along the x, y and z directions, corresponding to directions along the momentum transfer $\mathbf{Q}$, perpendicular to $\mathbf{Q}$ but in the (h, h, l) plane, and perpendicular to the scattering plane, respectively. For this configuration, the SF cross-section $\sigma_x^{SF}(\mathbf{Q}) \approx M_z + M_y$, where M_y and M_z are magnetic fluctuations along the local y and z directions, respectively, for systems with large magnetic moments. Correspondingly, $\sigma_z^{SF}(\mathbf{Q}) \approx M_y$ and $\sigma_z^{NSF}(\mathbf{Q}) \approx M_z$. **d**, Schematic of the phase diagram for the nearest-neighbour XYZ model[63] in the experimentally relevant quadrants for $Ce_2Zr_2O_7$. The labels X-AIAO, Y-AIAO and Z-AIAO represent all-in–all-out magnetic order along the local x, y and z axes, respectively. The red square denotes the parameterization from ref. 49, and the blue triangle and blue star are the ones from ref. 54. For the parameters in π-D-QSI, the photon can be observed in the neutron scattering cross-section, but it cannot be observed for parameters in the π-O-QSI phase. In both cases, the spinons produce a small quasielastic peak from thermal excitations and three inelastic peaks of decreasing intensities. **e**, Tunnelling process between different spin-ice configurations that form the coherent photon excitation. A vector pointing out of an up tetrahedron (in blue) is a representation of a positive pseudospin component for the one with the largest coupling $|S^{\parallel}| = +1/2\rangle$ and a vector pointing out is $|S^{\parallel}| = -1/2\rangle$. **f**, When flipping a spin, one violates the ice rules and creates spinons that live at the centre of the neighboring tetrahedra and are sources of the emergent electric field.

constraints, known as the ice rules, is imposed on every tetrahedron and can be mapped to a divergence-less coarse-grained spin field $\mathscr{E}$. Defect tetrahedra in which the local ice rules are violated then behave as mobile charged excitations interacting electrostatically through this emergent field. This structure leads to 'pinch points' in the momentum transfer $\mathbf{Q}$ dependence of the spin–spin correlation function $S(\mathbf{Q})$. The pinch points can be revealed in polarized neutron scattering experiments with neutrons polarized along the z axis perpendicular to the $(h, h, 0) \times (0, 0, l)$ scattering plane[22–24] (Fig. 1c). These results showcase the usefulness of polarized neutron scattering in unveiling exotic emergent physics and its connection to microscopic descriptions.

For $S = 1/2$ pyrochlore magnets in which quantum effects are important, the CSI is theoretically predicted to be promoted to a quantum spin ice (QSI)[25], a QSL in which the low-energy dynamics of the two-in–two-out manifold is described by compact quantum electrodynamics[26–32]. This implies that a QSI hosts gapless excitations, dubbed photons, with a linear dispersion that describes coherent fluctuations within the spin-ice manifold (Fig. 1e), in addition to the spinons at higher energies[25,26,30]. These linearly dispersing gapless bosonic modes should be detectable by a characteristic T^3 contribution to the low-temperature heat capacity[26,30,33]. A QSI also supports massive $S = 1/2$ spinon excitations that are the quantum analogue of the defect tetrahedra in CSI (Fig. 1f) and gapped topological defects known as visons[25]. The experimental discovery of a material realization of QSI is an outstanding problem that—despite encouraging results[34–37]—has yet to receive any definitive evidence. Recently, 3D pyrochlore systems $Ce_2M_2O_7$ (M = Sn, Zr or Hf; Extended Data Fig. 1) have been suggested as effective $S = 1/2$ QSI candidates[38–45], but there has been no conclusive evidence of quasielastic magnetic scattering signals from photons, a key signature for a QSI.

Here we use polarized neutron scattering experiments and low-temperature specific heat measurements on single crystals of $Ce_2Zr_2O_7$ and show that all the results are consistent with the presence of magnetic excitations near zero energy at 33–50 mK in addition to signatures of spinons at higher energies, and the heat capacity data are consistent with the T^3 dependence expected for linearly dispersing gapless bosonic modes[26,30,33]. By comparing the energy (E), momentum transfer ($\mathbf{Q}$) and polarization dependencies of magnetic excitations with theoretical calculations[46–52], we conclude that $Ce_2Zr_2O_7$ is a strong candidate for a dipolar–octupolar π-flux QSI[50] with dominant dipolar Ising interactions.

Experimental and theoretical results

Ce^{3+} ($4f^1$, $^2F_{5/2}$) magnetically active ions in the crystal field of eight oxygen anions of $Ce_2Zr_2O_7$ form an effective $S = 1/2$ Kramers doublet.

https://doi.org/10.1038/s41567-025-02922-9

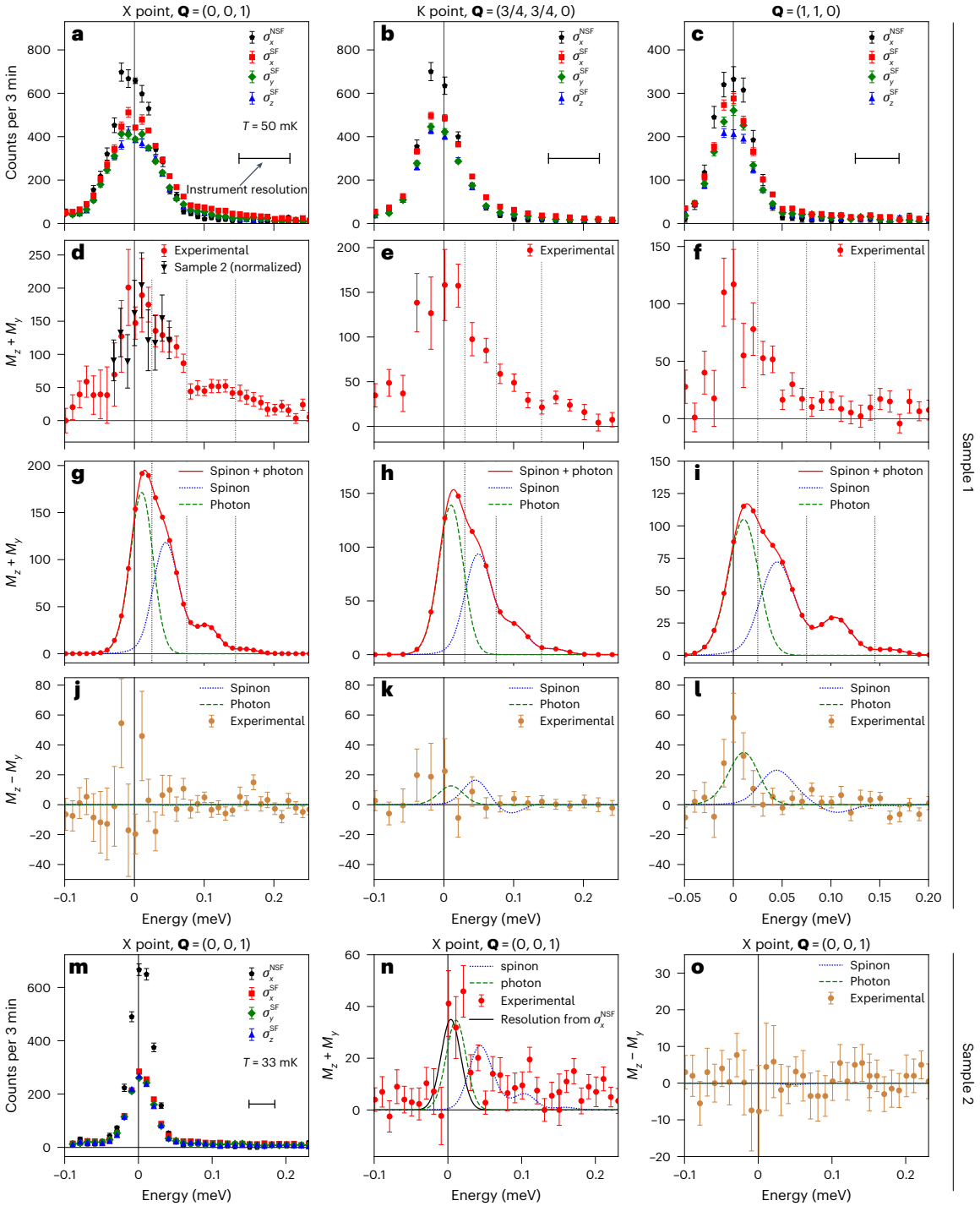

Fig. 2 | Energy scans of the polarized neutron scattering cross-sections at different momentum positions for $Ce_2Zr_2O_7$. **a**–**c**, Neutron scattering cross-sections for different polarizations as a function of energy at **Q** = (0, 0, 1) (X point; **a**), **Q** = (3/4, 3/4, 0) (K point; **b**) and **Q** = (1, 1, 0) (**c**). **d**–**f**, Total magnetic scattering $M_z + M_y$ for samples 1 and 2 at X point (**d**), sample 1 at K point (**e**) and sample 1 at **Q** = (1, 1, 0) (**f**). **g**–**i**, Theoretical fit to $M_z + M_y$ using GMFT for the spinons and Gaussian quantum electrodynamics for the photons at X point (**g**), K point (**h**) and **Q** = (1, 1, 0) (**i**). **j**–**l**, Polarization anisotropy $M_z - M_y$ and theoretical prediction for the spinon and photon contributions to it at X point (**j**), K point (**k**) and **Q** = (1, 1, 0) (**l**). **m**, The raw NSF and SF neutron scattering cross-sections for sample 2 at X point and 33 mK. **n**, Total magnetic scattering $M_z + M_y$ for sample 2 at X point. Theoretical fit to $M_z + M_y$ using GMFT for the spinons and Gaussian quantum electrodynamics for the photons at X point. **o**, Polarization anisotropy $M_z - M_y$ and theoretical prediction for the spinon and photon contributions to it at **Q** = (0, 0, 1). A direct comparison between samples 1 and 2 with the same energy resolution is shown in **d**. The black line in **n** is the experimental resolution obtained by fitting a Gaussian to $\sigma_x^{NSF}(E)$. The theoretical results were produced using $\mathcal{J}_x = 0.076$ meV, $(\mathcal{J}_y + \mathcal{J}_z)/4 = 0.021$ meV and $\hbar c_{QSI}/a_0 = 0.0028$ meV ($c_{QSI} = 4.6$ m s^{-1}). To incorporate a finite experimental resolution, the results are broadened using a Gaussian with FWHM values of 0.04 meV, 0.04 meV and 0.035 meV at the X, K and **Q** = (1, 1, 0) points, respectively, for sample 1 and of 0.035 meV at the X point for sample 2. The vertical dotted lines in **d**–**i** are guides to the eye to denote the transitions from the quasielastic photon signal to the first spinon peak and between the three spinon peaks of π-flux QSI. The vertical error bars in **a**–**c** and **m** are statistical errors of one standard deviation. The horizontal bars in **a**–**c** and **m** are the instrumental energy resolutions in FHWM as determined from the energy width of $\sigma_x^{NSF}(E)$. Data in **a** and **b** are obtained with $E_f = 3.23$ meV, whereas in **c** and **m**, they are obtained with $E_f = 2.51$ meV. The vertical error bars in **d**–**f**, **j**–**l**, **n** and **o** are propagating errors using equation (3).

https://doi.org/10.1038/s41567-025-02922-9

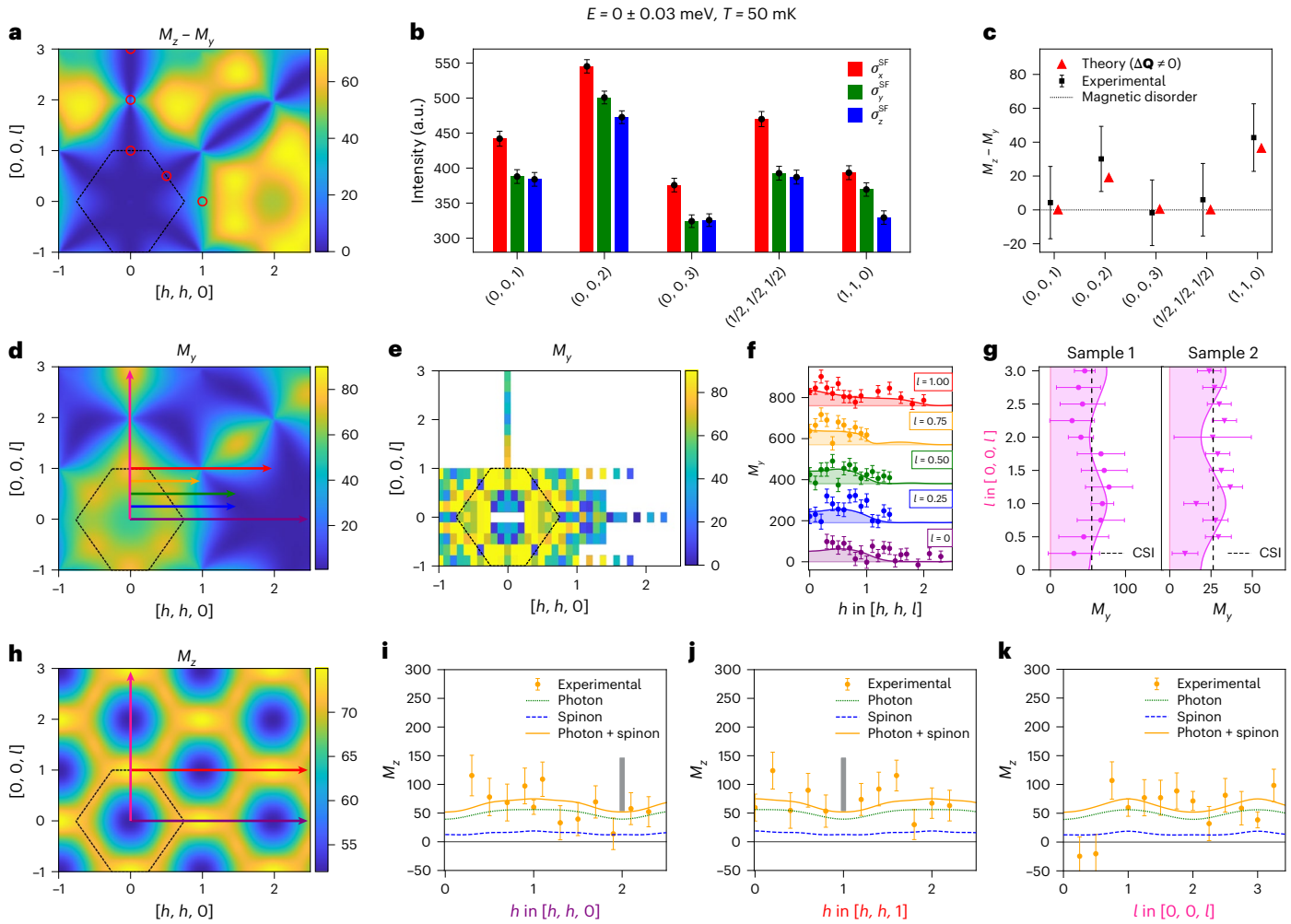

Fig. 3 | Wavevector and polarization dependencies of magnetic scattering at $E = 0 \pm 0.03$ meV for $Ce_2Zr_2O_7$. **a**, Theoretical prediction for the polarization anisotropy $M_z - M_y$ from the total of spinons and photons at the elastic line $E = 0 \pm 0.03$ meV in the $[h, h, l]$ scattering plane using $\hbar c_{QSI}/a_0 = 0.0028$ meV ($c_{QSI} = 4.6$ m s^{-1}). **b**, $\sigma^{SF}_{x,y,z}(\mathbf{Q})$ at various momentum positions highlighted by red circles in **a**. **c**, Comparison between theory with a small momentum uncertainty (that is, $\Delta Q \neq 0$) and experiments for the polarization anisotropy. **d**,**e**, Theoretical predictions (**d**) and measurements (**e**) of M_y in the $[h, h, l]$ scattering plane. The colour bar in **e** is capped off to allow for better comparison with theory. **f**,**g**, Comparison between measurements and theoretical predictions for M_y along the $[h, h, l]$ directions with $l = 0$, 0.25, 0.5, 0.75 and 1 (**f**), and along the $[0, 0, l]$ direction for samples 1 and 2 (**g**). They are indicated by arrows in **d**. The results in **f** are shifted vertically for clarity. The results in **g** are compared with CSI. **h**, Theoretical predictions of M_z in the $[h, h, l]$ scattering plane. **i**–**k**, M_z along the $[h, h, 0]$ (**i**), $[h, h, 1]$ (**j**) and $[0, 0, l]$ (**k**) directions, and the theoretical calculation for the contributions from spinons, photons and their total. These lines are indicated by arrows in **d**. The grey windows in **i** and **j** indicate the nuclear Bragg peaks at the (1, 1, 1) and (2, 2, 0) points. The vertical error bars in **c**, **f**, **g** and **i**–**k** are propagating errors using equation (3). Data in **b**, **c**, **e**–**g** and **i**–**k** are obtained with $E_f = 3.23$ meV. The vertical error bars in **b** are statistical errors of one standard deviation. All measurements are on sample 1 except the second panel of **g**.

The doublets can be modelled as pseudospins-1/2 in which the x and z components of the pseudospin (τ^x and τ^z) transform as magnetic dipoles, whereas the y component (τ^y) transforms as a magnetic octupole[46,47]. The x component is referred to as a dipole despite having an octupolar magnetic charge density (Fig. 1a) because of its transformation property. The most general nearest-neighbour Hamiltonian for these dipolar–octupolar pseudospin systems is

$$\mathcal{H} = \sum_{a\in\{x,y,z\}} \sum_{\langle i,j\rangle} J_{aa} \tau_i^a \tau_j^a + \sum_{\langle i,j\rangle} J_{xz} \left(\tau_i^x \tau_j^z + \tau_i^z \tau_j^x\right), \quad (1)$$

where the pseudospin components are defined in sublattice-dependent local coordinates. By performing a local rotation about the y axis, the system can be brought to the simple XYZ form as

$$\mathcal{H} = \sum_{a\in\{x,y,z\}} \sum_{\langle i,j\rangle} \mathcal{J}_a S_i^a S_j^a, \quad (2)$$

with the pseudospins $S^x = \cos\theta\tau^x - \sin\theta\tau^z$, $S^y = \tau^y$ and $S^z = \sin\theta\tau^x + \cos\theta\tau^z$. When the dipolar–octupolar system stabilizes QSI, the XYZ model can be mapped to lattice quantum electrodynamics by associating the pseudospin component with the dominant coupling $\mathcal{J}_{||} = \max(\mathcal{J}_x, \mathcal{J}_y, \mathcal{J}_z)$ to the emergent electric field $\mathscr{E}$, that is, $S_i^{||} = \mathscr{E}_{r,r'}$, and the transverse parts to spinon bilinears dressed with the emergent photon $S_i^+ = \frac{1}{2}\Phi_r^\dagger e^{i\mathscr{A}_{r,r'}}\Phi_{r'}$. Here S^+ is the raising operator in the $S^{||}$ basis, r and r' label the centres of the tetrahedron such that the site i sits at the centre of the link $r \to r'$ joining them, $\Phi_r^\dagger$ is a spinon creation operator and $\mathscr{A}$ is the vector potential canonically conjugate to the $\mathscr{E}$ field.

Depending on the leading coupling $\mathcal{J}_{||}$, drastically different responses are expected in inelastic neutron scattering (INS) experiments. Indeed, $Ce_2Zr_2O_7$ has an anisotropic g tensor with $g_{zz} = 2.57$ and $g_{xx} = g_{yy} = 0$ such that the magnetic field linearly couples only to τ^z (refs. 38,39). As a result, neutron scattering cross-sections σ are only sensitive to correlations between τ^z for small momentum transfer $\sigma \propto \langle\tau^z\tau^z\rangle \propto \cos^2\theta\langle S^zS^z\rangle + \sin^2\theta\langle S^xS^x\rangle$ (ref. 41). If $\mathcal{J}_{||} = \mathcal{J}_y > \mathcal{J}_x, \mathcal{J}_z$, INS probes the

https://doi.org/10.1038/s41567-025-02922-9

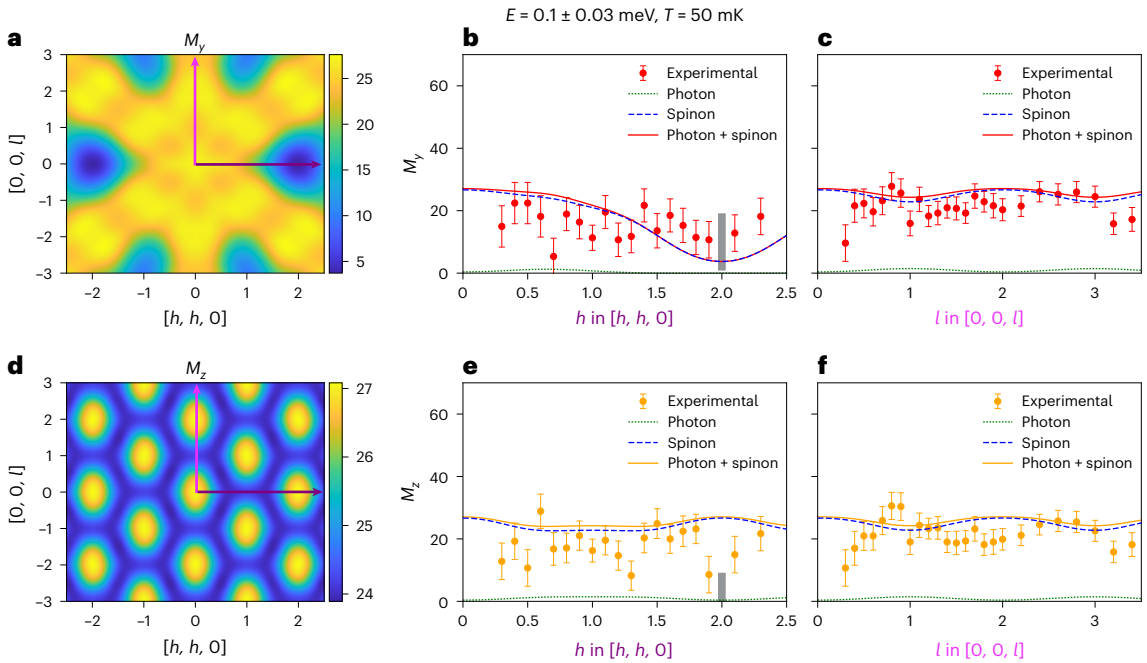

Fig. 4 | Wavevector and polarization dependencies of magnetic scattering at $E = 0.1 \pm 0.03$ meV for $Ce_2Zr_2O_7$. a,**d**, Theoretical predictions for M_y (**a**) and M_z (**d**) from the total of spinons and photons at $E = 0.1 \pm 0.03$ meV in the $[h, h, l]$ scattering plane using $\hbar c_{QSI}/a_0 = 0.0028$ meV ($c_{QSI} = 4.6$ m s^{-1}). **b**,**c**, M_y along the $[h, h, 0]$ (**b**) and $[0, 0, l]$ (**c**) directions and the theoretical predictions for the contributions from spinons, photons and their total. These lines are indicated by arrows in **a**. **e**,**f**, M_z along the $[h, h, 0]$ (**e**) and $[0, 0, l]$ (**f**) directions and the theoretical predictions for the contributions from spinons, photons and their total. These lines are indicated by arrows in **d**. The grey windows in **b** and **e** indicate the nuclear Bragg peak (2, 2, 0). The vertical error bars in **b**, **c**, **e** and **f** are propagating errors obtained using equation (3). Data in **b**, **c**, **e** and **f** are obtained with $E_f = 3.23$ meV. Measurements are performed on sample 1.

two-spinon continuum $\sigma \propto \cos^2(\theta)\langle\Phi^\dagger\Phi\Phi^\dagger\Phi\rangle + \sin^2(\theta)\langle\Phi^\dagger\Phi\Phi^\dagger\Phi\rangle$, whereas the photon remains invisible. By contrast, for $\mathcal{J}_{||} = \mathcal{J}_x > \mathcal{J}_y, \mathcal{J}_z$, both photons and spinons should be observable provided there is a non-zero off-diagonal term $\theta \neq 0$ (that is, $J_{xz} \neq 0$) since $\sigma \propto \cos^2(\theta)\langle\Phi^\dagger\Phi\Phi^\dagger\Phi\rangle + \sin^2(\theta)\langle\mathscr{E}\mathscr{E}\rangle$. Identifying a quasielastic signal from the photons, thus, provides a method to obtain information about the underlying microscopic couplings of a dipolar–octupolar QSI (Fig. 1d).

Previous investigations of $Ce_2Zr_2O_7$ have suggested that it stabilizes a QSI as its ground state. Heat capacity measured down to ~50 mK, magnetic susceptibility and muon spin relaxation found no sign of magnetic order or spin freezing above 20 mK (refs. 38,39,42,53–55). Further detailed theoretical fits to thermodynamic measurements have determined the microscopic couplings, indicating that the system is in a region of parameter space that is theoretically suggested to host a specific flavour of QSI known as the π-flux quantum spin ice (π-QSI), where a static π-flux of the emergent gauge field threads the hexagonal plaquette of the pyrochlore lattice ($\nabla \times \mathscr{A} = \pi$). The other stable QSL in the phase diagram, 0-flux QSI (0-QSI) (Fig. 1d), only has vanishing fluxes ($\nabla \times \mathscr{A} = 0$). In particular, one investigation found that the leading coupling is between the octupolar components S^y (ref. 49), whereas another puts $Ce_2Zr_2O_7$ at the boundary (that is, $\mathcal{J}_y \approx \mathcal{J}_x > \mathcal{J}_z$) between the π-flux QSI with dominant dipolar (π-D-QSI) and dominant octupolar (π-O-QSI) coupling[54] (Fig. 1d). INS should be able to differentiate between these two cases since the photon will not be visible in π-O-QSI but should produce a visible quasielastic signal for π-D-QSI if $\theta \neq 0$.

In previous experiments on $Ce_2Zr_2O_7$ and $Ce_2Sn_2O_7$, unpolarized or polarized neutron scattering with only one neutron polarization direction was carried out at base ($T = 35$–100 mK) and high ($T = 10$ K) temperatures. Then, the magnetic signal was extracted by taking the temperature difference in scattering signals between the base and high temperatures[38–42,53,54,56]. This method reveals a broad continuum consistent with a two-spinon continuum and no magnetic signal at the elastic position $E \approx 0$ meV. In particular, recent measurements on $Ce_2Sn_2O_7$ have revealed the presence of three inelastic peaks of decreasing intensity in the continuum[56], a signature of π-flux QSI[52] (Fig. 1d). Although such measurements are consistent with π-O-QSI, determining the existence/absence of a quasielastic magnetic signal is an involved task that requires careful consideration. The assumption in isolating the magnetic signal by temperature subtraction is that the non-magnetic scattering is temperature independent between the base and high temperatures[38–42,53,54,56]. Although such an assumption might be reasonable for CSI in which magnetic scattering is much larger than the non-magnetic contributions due to the large effective moment[22–24], it is unclear that the temperature difference method[38–42,53,54,56] can effectively extract the magnetic signal in the low-energy region, near $E \approx 0$, for an $S = 1/2$ system with a potentially large non-magnetic scattering background.

A conclusive way to isolate the E and $\mathbf{Q}$ dependencies of magnetic scattering in a material is the full neutron polarization analysis[57–59]. By polarizing the incident-beam neutrons along the directions of x axis (parallel to $\mathbf{Q}$), y axis (perpendicular to $\mathbf{Q}$ in the scattering plane) and z axis (perpendicular to the scattering plane), the neutron spin-flip (SF) and non-spin-flip (NSF) scattering cross-sections at $\mathbf{Q}$ and E for the x, y or z polarization direction are $\sigma^{SF}_{x,y,z}(\mathbf{Q}, E)$ and $\sigma^{NSF}_{x,y,z}(\mathbf{Q}, E)$, respectively (Fig. 1c). They are related to the magnetic scattering along the y and z directions M_y and M_z, respectively, via[59]

$$\begin{pmatrix} \sigma_x^{SF} \\ \sigma_y^{SF} \\ \sigma_z^{SF} \\ \sigma_x^{NSF} \\ \sigma_y^{NSF} \\ \sigma_z^{NSF} \end{pmatrix} = \frac{1}{R+1} \begin{pmatrix} R & R & 1 & (2R+1)/3 & (R+1) \\ 1 & R & 1 & (2R+1)/3 & (R+1) \\ R & 1 & 1 & (2R+1)/3 & (R+1) \\ 1 & 1 & R & (R+2)/3 & (R+1) \\ R & 1 & R & (R+2)/3 & (R+1) \\ 1 & R & R & (R+2)/3 & (R+1) \end{pmatrix} \begin{pmatrix} M_y \\ M_z \\ N \\ \mathrm{NSI} \\ B \end{pmatrix}, \quad (3)$$

where R is the imperfect neutron polarization quantified by measuring the nuclear Bragg peaks contamination into the SF channel ($R = \frac{\mathrm{NSF}_N}{\mathrm{SF}_N} \approx 30$ in our experiments), N is the nuclear coherent scattering (including temperature-dependent phonon scattering), NSI is the $\mathbf{Q}$-independent nuclear spin incoherent scattering (NSI $\ll N$) and B is the background scattering. For polarized neutron scattering experiments measuring only $\sigma_z^{\mathrm{SF}}(\mathbf{Q})$ and $\sigma_z^{\mathrm{NSF}}(\mathbf{Q})$ (refs. 24,42), both channels would have significant NSI + B scattering, and $\sigma_z^{\mathrm{NSF}}(\mathbf{Q})$ would also have a nearly full N contribution. For CSI systems such as $Ho_2Ti_2O_7$ with large local moments (M_y, $M_z \gg N$, NSI, B), one can approximate $\sigma_z^{\mathrm{SF}}(\mathbf{Q}) \approx M_y$ and $\sigma_z^{\mathrm{NSF}}(\mathbf{Q}) \approx M_z$ (ref. 24). However, for the effective $S = 1/2$ system such as $Ce_2Zr_2O_7$, there is no determination of the intensity ratio between M_y, M_z and N, NSI, B at different temperatures[42]. Therefore, full neutron polarization analysis by measuring $\sigma_{x,y,z}^{\mathrm{SF}}(\mathbf{Q}, E)$ and $\sigma_x^{\mathrm{NSF}}(\mathbf{Q}, E)$ is necessary to conclusively separate the magnetic scattering from N, NSI and B without the need to use high-temperature measurements to estimate the background scattering[42].

Figure 2a shows the energy scans of $\sigma_{x,y,z}^{\mathrm{SF}}(\mathbf{Q}, E)$ and $\sigma_x^{\mathrm{NSF}}(\mathbf{Q}, E)$ at $\mathbf{Q} = (0, 0, 1)$ and $T = 50$ mK. Near the elastic position ($E = 0 \pm 0.03$ meV; Extended Data Fig. 2), we find $\sigma_x^{\mathrm{NSF}} > \sigma_x^{\mathrm{SF}} > \sigma_y^{\mathrm{SF}} \approx \sigma_z^{\mathrm{SF}}$. At the inelastic position at which previous unpolarized INS work found spin excitation continuum around $E = 0.12$ meV (refs. 38,39), we have $\sigma_x^{\mathrm{SF}} > \sigma_y^{\mathrm{SF}} \approx \sigma_z^{\mathrm{SF}} > \sigma_x^{\mathrm{NSF}}$. The energy dependence of $M_z + M_y$ determined using $\sigma_{x,y,z}^{\mathrm{SF}}$ in equation (2a) and equation (3) reveals 3 distinct peaks at $E \approx 0$, 0.05 and 0.12 meV, with dominating magnetic scattering at $E = 0 \pm 0.03$ meV (Fig. 2d). Furthermore, $M_z - M_y \approx 0$ (Fig. 2j) indicates that magnetic scattering at the probed energies is isotropic in spin space. Although the magnetic intensity around $E \approx 0.12$ meV is consistent with unpolarized INS measurements[38,39], the discovery of dominating magnetic scattering near zero energy cannot be obtained from previous work[38–42,53,54,56]. Since unpolarized neutron scattering measures $\sigma_x^{\mathrm{NSF}} + \sigma_x^{\mathrm{SF}}$, we estimate that $M_z + M_y$ is about 10% and 75% of the total scattering near the elastic position and $E = 0.12$ meV, respectively (Fig. 2d). Figure 2b,c summarizes the energy scans of $\sigma_{x,y,z}^{\mathrm{SF}}(\mathbf{Q}, E)$ and $\sigma_x^{\mathrm{NSF}}(\mathbf{Q}, E)$ at $\mathbf{Q} = (3/4, 3/4, 0)$ and $\mathbf{Q} = (1, 1, 0)$, respectively. The estimated $M_z + M_y$ and $M_z - M_y$ are shown in Fig. 2e,k, respectively, for $\mathbf{Q} = (3/4, 3/4, 0)$. Similar results, obtained with better instrumental energy resolution, are shown in Fig. 2f,l. Although magnetic scattering at the X and K points are isotropic in spin space at the probed energies (Fig. 2j,k and Extended Data Figs. 3 and 4), the quasielastic magnetic scattering at $\mathbf{Q} = (1, 1, 0)$ is clearly anisotropic with $M_z - M_y > 0$ (Fig. 2l and Supplementary Tables 1–5). To verify the results' reproducibility and determine the energy scale of quasielastic magnetic scattering, we have performed similar measurements on a second sample at the X point at $\mathbf{Q} = (0, 0, 1)$ with a higher energy resolution (0.035-meV full-width at half-maximum (FWHM)) and at a lower temperature ($T = 33$ mK). The results shown in Fig. 2m–o confirm the presence of a dominant quasielastic peak near 0.01 meV in the total magnetic scattering (Fig. 2n) and the absence of polarization anisotropy at the X point (Fig. 2o and Extended Data Figs. 6–8).

To understand these results, we model the spinon dynamics using the framework of gauge mean-field theory (GMFT)[33,51,52,60–62] and describe the photons using Gaussian quantum electrodynamics[26,30] (Methods). Assuming such an emergent quantum electrodynamics description, the dominant quasielastic signal is then explained by the emergent photons. We reach this conclusion since the dominant quasielastic signal cannot be accounted for by only invoking the spinon contribution (Methods). As already emphasized, the observation of a signal coming from the emergent photons implies that $\mathcal{J}_x > \mathcal{J}_y, \mathcal{J}_z$ and $\theta \neq 0$ (π-D-QSI regime).

We fit the experimental results by tuning the microscopic couplings and the speed of the emergent photon to obtain the theoretical predictions (Fig. 2g–l). The theoretical modelling predicts a series of peaks in the total magnetic scattering $M_z + M_y$. The first quasielastic one comes from photons, and then the spinons produce three others of decreasing intensity (the third is extremely faint). These three inelastic spinon peaks are a unique and distinctive signature of π-flux QSI[52]. By contrast, in 0-flux QSI, spinons produce a broad inelastic continuum with a single local maximum. The predicted transitions are clearly observed at $\mathbf{Q} = (0, 0, 1)$ (Fig. 2d and Extended Data Fig. 5). At this point, there is a transition from the photon contributions to the first spinon peak at around $E \approx 0.025$ meV and then a second one from the first to the second spinon peak at $E \approx 0.075$ meV. Our model is consistent with the position of these transitions and the decreasing intensity of the corresponding peaks. For the polarization difference $M_z - M_y$, theory predicts that there should not be any anisotropy at $\mathbf{Q} = (0, 0, 1)$, a small response at $\mathbf{Q} = (3/4, 3/4, 0)$ and the most intense signal at $\mathbf{Q} = (1, 1, 0)$, which is once again consistent with the measurements (Fig. 2j–l,o). In particular, at $\mathbf{Q} = (1, 1, 0)$ (Fig. 2l), the anisotropic quasielastic response is well accounted for by the photon. The main discrepancy is that the model predicts a finite $M_z - M_y$ value at $\mathbf{Q} = (1, 1, 0)$ in the inelastic spinon contribution, which is not seen in the experiment. This could potentially be attributed to effects beyond GMFT, such as thermally excited fluxes or spinon–photon interactions. Measurements on the second sample are also well reproduced by the same model (Fig. 2n,o) without introducing any additional fitting parameter besides an overall scaling factor. In short, the energy scans provide evidence for a substantial quasielastic signal with the same momentum-dependent polarization anisotropy as predicted for the emergent photon, as well as multiple inelastic peaks consistent with the two-spinon continuum of π-flux QSI.

To further investigate if the quasielastic signal is compatible with the emergent photon, we e xamine its momentum dependence (Fig. 3). Figure 3b,c presents the raw $\sigma_{x,y,z}^{\mathrm{SF}}(\mathbf{Q})$ data and the resulting polarization anisotropy $M_z - M_y$ at a specified $\mathbf{Q}$ value with $E = 0 \pm 0.03$ meV. The quasielastic signal displays clear momentum and polarization dependencies with $M_z > M_y$ at $\mathbf{Q} = (1, 1, 0)$, inconsistent with conventional strong magnetic disorder (that is, glassiness), where one would expect a polarization- and momentum-independent signal (that is, $M_z \approx M_y$ at all $\mathbf{Q}$ values; Methods). By contrast, our modelling using emergent spinons and photons properly captures the observed spin-space anisotropy (Fig. 3a–c).

Figure 3d,h shows the calculated $\mathbf{Q}$ dependence of M_y and M_z at $E = 0 \pm 0.03$ meV, respectively (Extended Data Fig. 3). The calculations predict intense scattering along the first Brillouin zone boundary for M_y and a mostly momentum-independent signal for M_z. These are compared with the measurements of M_y (Fig. 3e–g) and M_z (Fig. 3i–k). Both comparisons show that the GMFT and Gaussian quantum electrodynamics effectively reproduce the momentum and polarization dependencies of the magnetic scattering. In particular, Fig. 3e,g shows a depletion of M_y at the zone centre and oscillations along the $[0, 0, l]$ direction. These observations are often taken as signatures of QSI given that one expects a flat M_y signal at the zone centre and along $[0, 0, l]$ for CSI[22–24,30,36,38] (Fig. 3g). We have carried out these measurements on two different $Ce_2Zr_2O_7$ samples, and the results are consistent with each other (Fig. 3g). Since the magnetic scattering near the elastic line is dominated by the photon (Fig. 3i–k), we fit these measurements to determine an optimal speed of light of $\hbar c_{\mathrm{QSI}}/a_0 = 0.0028$ meV, where a_0 is the lattice constant.

Figure 4a,d shows the calculated $\mathbf{Q}$ dependence of M_y and M_z at $E = 0.1 \pm 0.03$ meV in the (h, h, l) zone, respectively (Extended Data Fig. 3). Compared with Fig. 2, this momentum scan is centred around the second spinon peak and is, thus, dominated by spinons with only negligible photon scattering. The comparison of experimentally estimated M_y and M_z with theoretical calculations along the $[0, 0, l]$ and $[h, h, 0]$ directions are summarized in Fig. 4b,c and Fig. 4e,f, respectively. Note that the theoretical calculations are scaled consistently with the data in Figs. 2–4. These results, thus, show that on top of giving a reasonable qualitative agreement for the polarization and momentum dependencies of the inelastic magnetic scattering, our description in

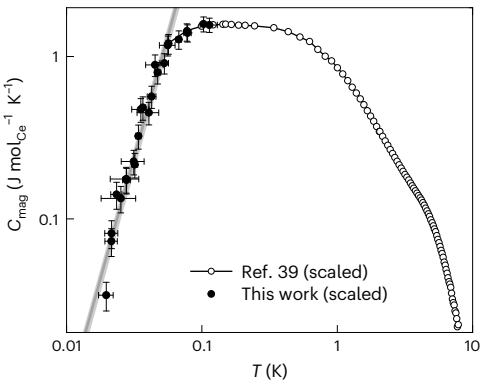

Fig. 5 | Specific heat of $Ce_2Zr_2O_7$. Low-temperature data of the present work (full black points) together with previously published data[39] (open symbols), both scaled to the mean value of previously published data[39,42] at 100 mK (Extended Data Fig. 9e, star). The grey line is a fit to the data below 50 mK with a slope of 3, corresponding to a cubic-in-temperature specific heat. The vertical error bars are estimated to be at a maximum of 10% at 100 mK and up to 20% at the lowest temperatures. The horizontal error bars represent the maximum errors in the temperatures of the sample, which amount to 10% on average (depending on whether a larger or smaller heater power was used).

terms of emergent quantum electrodynamics quantitatively reproduces the intensity ratio between the elastic and inelastic signals at $E \approx 0.1$ meV (Extended Data Figs. 6–8).

Finally, we have performed specific heat measurements with a setup (Extended Data Fig. 9) that can reach temperatures below the previous low-temperature limit of ~50 mK (refs. 39,42). The data decrease monotonically down to the lowest temperature, evidencing the absence of a phase transition (Fig. 5). This is in agreement with previous muon spin relaxation experiments[39,55] and represents further support for a non-magnetically ordered ground state. The temperature dependence at the lowest temperatures is well captured by a T^3 power law, as shown by the straight line with a slope of 3 on the double-logarithmic scale (Fig. 5). This behaviour is expected for the photon-like excitation associated with the QSI, thereby presenting further evidence for this state. We note that the low-temperature specific heat data can also be equally well fit by an activated exponential form. However, as detailed in Methods ('Quality of fits to the specific heat data') and Extended Data Fig. 9, the power-law fit provides a better physical description of the system. We, therefore, adopt the cubic fit consistent with gapless photon excitations expected in a QSI. The photon velocity extracted from the slope of this cubic scaling is $\hbar c_{QSI}/a_0 = 0.0049 \pm 0.0002$ meV, a value of the same order as the one obtained from fitting the neutron scattering results. The integrated magnetic entropy is somewhat smaller than the full entropy $\bar{R}\ln 2$ (Extended Data Fig. 9h), where $\bar{R}$ is the universal gas constant, but still consistent with the full value within the error bars of the experiments.

Summary

We performed full polarization analysis of INS experiments on the 3D pyrochlore lattice QSI candidate $Ce_2Zr_2O_7$ and have discovered a continuum of quasielastic magnetic scattering near $E = 0$. This signal is incompatible with a spinon continuum at higher energy but consistent with the emergent photon predicted to exist in QSI[25,26,30]. Such an observation also sheds light on microscopic couplings since the presence of photons would indicate the ground state is π-D-QSI. We have further highlighted that the multiple-peak structure of the inelastic signal and the momentum dependence of the intensity profile display the key features of π-QSI. Although current polarized neutron scattering technology does not allow higher-resolution measurements to determine the linear dispersion expected for photon scattering, the cubic scaling of the low-temperature heat capacity measurements (Fig. 5) offers further supporting evidence for their presence. Future investigations on the role of disorder and neutron scattering experiments with even greater energy resolution would be highly desirable to draw definitive conclusions on the nature of the observed quasielastic signal. In any case, our work, combined with previous experimental investigations[38,39,42,53–55], lends strong support to the identification of $Ce_2Zr_2O_7$ as an experimental realization of QSI—one of the most paradigmatic QSL in condensed-matter physics.

Online content

Any methods, additional references, Nature Portfolio reporting summaries, source data, extended data, supplementary information, acknowledgements, peer review information; details of author contributions and competing interests; and statements of data and code availability are available at https://doi.org/10.1038/s41567-025-02922-9.

References

1. Gardner, J. S., Gingras, M. J. P. & Greedan, J. E. Magnetic pyrochlore oxides. *Rev. Mod. Phys.* **82**, 53–107 (2010).
2. Savary, L. & Balents, L. Quantum spin liquids: a review. *Rep. Prog. Phys.* **80**, 016502 (2017).
3. Zhou, Y., Kanoda, K. & Ng, T.-K. Quantum spin liquid states. *Rev. Mod. Phys.* **89**, 025003 (2017).
4. Hallas, A. M., Gaudet, J. & Gaulin, B. D. in *Annual Review of Condensed Matter Physics* Vol. 9 (eds Sachdev, S. & Marchetti, M. C.) 105–124 (Annual Reviews, 2018).
5. Broholm, C. et al. Quantum spin liquids. *Science* **367**, eaay0668 (2020).
6. Anderson, P. W. Resonating valence bonds: a new kind of insulator? *Mater. Res. Bull.* **8**, 153–160 (1973).
7. Anderson, P. W. The resonating valence bond state in La_2CuO_4 and superconductivity. *Science* **235**, 1196–1198 (1987).
8. Lee, P. A., Nagaosa, N. & Wen, X. G. Doping a Mott insulator: physics of high-temperature superconductivity. *Rev. Mod. Phys.* **78**, 17–85 (2006).
9. Kitaev, A. Y. Fault-tolerant quantum computation by anyons. *Ann. Phys.* **303**, 2–30 (2003).
10. Kitaev, A. Anyons in an exactly solved model and beyond. *Ann. Phys.* **321**, 2–111 (2006).
11. Takagi, H., Takayama, T., Jackeli, G., Khaliullin, G. & Nagler, S. E. Concept and realization of Kitaev quantum spin liquids. *Nat. Rev. Phys.* **1**, 264–280 (2019).
12. Han, T. H. et al. Fractionalized excitations in the spin-liquid state of a kagome-lattice antiferromagnet. *Nature* **492**, 406–410 (2012).
13. Norman, M. R. Colloquium: herbertsmithite and the search for the quantum spin liquid. *Rev. Mod. Phys.* **88**, 041002 (2016).
14. Shen, Y. et al. Evidence for a spinon Fermi surface in a triangular-lattice quantum-spin-liquid candidate. *Nature* **540**, 559–562 (2016).
15. Paddison, J. A. M. et al. Continuous excitations of the triangular-lattice quantum spin liquid $YbMgGaO_4$. *Nat. Phys.* **13**, 117–122 (2016).
16. Dai, P.-L. et al. Spinon Fermi surface spin liquid in a triangular lattice antiferromagnet $NaYbSe_2$. *Phys. Rev.* **11**, 021044 (2021).
17. Balz, C. et al. Physical realization of a quantum spin liquid based on a complex frustration mechanism. *Nat. Phys.* **12**, 942–947 (2016).
18. Scheie, A. O. et al. Proximate spin liquid and fractionalization in the triangular antiferromagnet $KYbSe_2$.*Nat. Phys.* **20**, 74–79 (2024).
19. Xie, T. et al. Complete field-induced spectral response of the spin-1/2 triangular-lattice antiferromagnet $CsYbSe_2$. *npj Quantum Mater.* **8**, 48 (2023).

20. Scheie, A. et al. Witnessing entanglement in quantum magnets using neutron scattering. *Phys. Rev. B* **103**, 224434 (2021).
21. Sherman, N. E., Dupont, M. & Moore, J. E. Spectral function of the J_1–J_2 Heisenberg model on the triangular lattice. *Phys. Rev. B* **107**, 165146 (2023).
22. Bramwell, S. T. & Gingras, M. J. P. Spin ice state in frustrated magnetic pyrochlore materials. *Science* **294**, 1495–1501 (2001).
23. Bramwell, S. T. & Harris, M. J. The history of spin ice. *J. Phys. Condens. Matter* **32**, 374010 (2020).
24. Fennell, T. et al. Magnetic Coulomb phase in the spin ice $Ho_2Ti_2O_7$. *Science* **326**, 415–417 (2009).
25. Gingras, M. J. P. & McClarty, P. A. Quantum spin ice: a search for gapless quantum spin liquids in pyrochlore magnets. *Rep. Prog. Phys.* **77**, 056501 (2014).
26. Hermele, M., Fisher, M. P. A. & Balents, L. Pyrochlore photons: the *U*(1) spin liquid in a *S*=1/2 three-dimensional frustrated magnet. *Phys. Rev. B* **69**, 064404 (2004).
27. Banerjee, A., Isakov, S. V., Damle, K. & Kim, Y. B. Unusual liquid state of hard-core bosons on the pyrochlore lattice. *Phys. Rev. Lett.* **100**, 047208 (2008).
28. Huang, C.-J., Deng, Y., Wan, Y. & Meng, Z. Y. Dynamics of topological excitations in a model quantum spin ice. *Phys. Rev. Lett.* **120**, 167202 (2018).
29. Kato, Y. & Onoda, S. Numerical evidence of quantum melting of spin ice: quantum-to-classical crossover. *Phys. Rev. Lett.* **115**, 077202 (2015).
30. Benton, O., Sikora, O. & Shannon, N. Seeing the light: experimental signatures of emergent electromagnetism in a quantum spin ice. *Phys. Rev. B* **86**, 075154 (2012).
31. Shannon, N., Sikora, O., Pollmann, F., Penc, K. & Fulde, P. Quantum ice: a quantum Monte Carlo study. *Phys. Rev. Lett.* **108**, 067204 (2012).
32. Pace, S. D., Morampudi, S. C., Moessner, R. & Laumann, C. R. Emergent fine structure constant of quantum spin ice is large. *Phys. Rev. Lett.* **127**, 117205 (2021).
33. Savary, L. & Balents, L. Coulombic quantum liquids in spin-1/2 pyrochlores. *Phys. Rev. Lett.* **108**, 037202 (2012).
34. Ross, K. A., Savary, L., Gaulin, B. D. & Balents, L. Quantum excitations in quantum spin ice. *Phys. Rev.* **1**, 021002 (2011).
35. Thompson, J. D. et al. Quasiparticle breakdown and spin Hamiltonian of the frustrated quantum pyrochlore $Yb_2Ti_2O_7$ in a magnetic field. *Phys. Rev. Lett.* **119**, 057203 (2017).
36. Sibille, R. et al. Experimental signatures of emergent quantum electrodynamics in $Pr_2Hf_2O_7$. *Nat. Phys.* **14**, 711–715 (2018).
37. Scheie, A. et al. Multiphase magnetism in $Yb_2Ti_2O_7$. *Proc. Natl Acad. Sci. USA* **117**, 27245–27254 (2020).
38. Gaudet, J. et al. Quantum spin ice dynamics in the dipole-octupole pyrochlore magnet $Ce_2Zr_2O_7$. *Phys. Rev. Lett.* **122**, 187201 (2019).
39. Gao, B. et al. Experimental signatures of a three-dimensional quantum spin liquid in effective spin-1/2 $Ce_2Zr_2O_7$ pyrochlore. *Nat. Phys.* **15**, 1052–1057 (2019).
40. Sibille, R. et al. Candidate quantum spin liquid in the Ce^{3+} pyrochlore stannate $Ce_2Sn_2O_7$. *Phys. Rev. Lett.* **115**, 097202 (2015).
41. Sibille, R. et al. A quantum liquid of magnetic octupoles on the pyrochlore lattice. *Nat. Phys.* **16**, 546–552 (2020).
42. Smith, E. M. et al. The case for a *U*(1) quantum spin liquid ground state in the dipole-octupole pyrochlore $Ce_2Zr_2O_7$. *Phys. Rev. X* **12**, 021015 (2022).
43. Porée, V. et al. Crystal-field states and defect levels in candidate quantum spin ice $Ce_2Hf_2O_7$. *Phys. Rev. Mater.* **6**, 044406 (2022).
44. Porée, V. et al. Dipolar-octupolar correlations and hierarchy of exchange interactions in $Ce_2Hf_2O_7$. Preprint at https://arxiv.org/abs/2305.08261 (2023).
45. Yahne, D. R. et al. Dipolar spin ice regime proximate to an all-in-all-out Néel ground state in the dipolar-octupolar pyrochlore $Ce_2Sn_2O_7$. *Phys. Rev. X* **14**, 011005 (2024).
46. Huang, Y.-P., Chen, G. & Hermele, M. Quantum spin ices and topological phases from dipolar-octupolar doublets on the pyrochlore lattice. *Phys. Rev. Lett.* **112**, 167203 (2014).
47. Li, Y.-D. & Chen, G. Symmetry enriched *U*(1) topological orders for dipole-octupole doublets on a pyrochlore lattice. *Phys. Rev. B* **95**, 041106 (2017).
48. Benton, O. Ground-state phase diagram of dipolar-octupolar pyrochlores. *Phys. Rev. B* **102**, 104408 (2020).
49. Bhardwaj, A. et al. Sleuthing out exotic quantum spin liquidity in the pyrochlore magnet $Ce_2Zr_2O_7$. *npj Quantum Mater.* **7**, 51 (2022).
50. Hosoi, M., Zhang, E. Z., Patri, A. S. & Kim, Y. B. Uncovering footprints of dipolar-octupolar quantum spin ice from neutron scattering signatures. *Phys. Rev. Lett.* **129**, 097202 (2022).
51. Desrochers, F., Chern, L. E. & Kim, Y. B. Symmetry fractionalization in the gauge mean-field theory of quantum spin ice. *Phys. Rev. B* **107**, 064404 (2023).
52. Desrochers, F. & Kim, Y. B. Spectroscopic signatures of fractionalization in octupolar quantum spin ice. *Phys. Rev. Lett.* **132**, 066502 (2024).
53. Gao, B. et al. Magnetic field effects in an octupolar quantum spin liquid candidate. *Phys. Rev. B* **106**, 094425 (2022).
54. Smith, E. M. et al. Quantum spin ice response to a magnetic field in the dipole-octupole pyrochlore $Ce_2Zr_2O_7$. *Phys. Rev. B* **108**, 054438 (2023).
55. Beare, J. et al. μSR study of the dipole-octupole quantum spin ice candidate $Ce_2Zr_2O_7$. *Phys. Rev. B* **108**, 174411 (2023).
56. Porée, V. et al. Evidence for fractional matter coupled to an emergent gauge field in a quantum spin ice. *Nat. Phys.* **21**, 83–88 (2024).
57. Moon, R. M., Riste, T. & Koehler, W. C. Polarization analysis of thermal-neutron scattering. *Phys. Rev.* **181**, 920–931 (1969).
58. Liu, P. et al. In-plane uniaxial pressure-induced out-of-plane antiferromagnetic moment and critical fluctuations in $BaFe_2As_2$. *Nat. Commun.* **11**, 5728 (2020).
59. Dai, P. Antiferromagnetic order and spin dynamics in iron-based superconductors. *Rev. Mod. Phys.* **87**, 855–896 (2015).
60. Lee, S., Onoda, S. & Balents, L. Generic quantum spin ice. *Phys. Rev. B* **86**, 104412 (2012).
61. Chen, G. Spectral periodicity of the spinon continuum in quantum spin ice. *Phys. Rev. B* **96**, 085136 (2017).
62. Yao, X.-P., Li, Y.-D. & Chen, G. Pyrochlore *U*(1) spin liquid of mixed-symmetry enrichments in magnetic fields. *Phys. Rev. Res.* **2**, 013334 (2020).
63. Patri, A. S., Hosoi, M. & Kim, Y. B. Distinguishing dipolar and octupolar quantum spin ices using contrasting magnetostriction signatures. *Phys. Rev. Res.* **2**, 023253 (2020).

Methods

Neutron scattering experiments

Single-crystal $Ce_2Zr_2O_7$ used for our experiments was described in detail in an earlier work[39]. Our polarized neutron scattering experiments were performed on the three-axis low-energy spectrometer (ThALES) at the Institut Laue Langevin. We carried out experiments on two crystals to confirm the results. One piece of single crystal (~2 g, sample 1) was mounted on a copper sample holder (Extended Data Fig. 1a). The crystal was prealigned using a laboratory X-ray Laue machine (Extended Data Fig. 1b), and then precisely aligned using the OrientExpress Laue neutron station at the Institut Laue Langevin. The mosaics of the (0, 0, 4) and (1, 1, 1) nuclear Bragg peaks were 1.87° ± 0.06° and 2.37° ± 0.24° FWHM, respectively. Sample 2 (~1.7 g) and its Laue pattern are shown in Extended Data Fig. 1c,d, respectively. The mosaic of the (1, 1, 1) peak of sample 2 is 2.85° ± 0.61° FWHM. The momentum transfer $\mathbf{Q}$ in 3D reciprocal space in $Å^{-1}$ was defined as $\mathbf{Q} = h\mathbf{a}^* + k\mathbf{b}^* + l\mathbf{c}^*$, where h, k and l are Miller indices and $\mathbf{a}^* = 2\pi(\mathbf{b}\times\mathbf{c})/[\mathbf{a}\cdot(\mathbf{b}\times\mathbf{c})]$, $\mathbf{b}^* = 2\pi(\mathbf{c}\times\mathbf{a})/[\mathbf{a}\cdot(\mathbf{b}\times\mathbf{c})]$ and $\mathbf{c}^* = 2\pi(\mathbf{a}\times\mathbf{b})/[\mathbf{a}\cdot(\mathbf{b}\times\mathbf{c})]$ with $\mathbf{a} = a_0\hat{\mathbf{x}}$, $\mathbf{b} = a_0\hat{\mathbf{y}}$, $\mathbf{c} = a_0\hat{\mathbf{z}}$ (where $a_0 = 10.70$ Å at room temperature is the lattice parameter, and $\hat{\mathbf{x}}$, $\hat{\mathbf{y}}$ and $\hat{\mathbf{z}}$ are unit vectors of the 3D Cartesian coordinate system) and the $Fd\bar{3}m$ space group (Fig. 1a). Sample 1 (sample 2) is aligned in the $(h, h, 0)\times(0, 0, l)$ scattering plane and mounted inside a dilution refrigerator kept at $T = 50$ mK ($T = 33$ mK) for the entire experiment (Fig. 1b). The final neutron energy was fixed at $E_f = 3.23$ meV or $E_f = 2.51$ meV, as specified in the figure caption. Both monochromator and analyser are horizontally and vertically focusing Heusler (1, 1, 1) crystals to produce and detect polarized neutrons. A flipping ratio measured on the (1, 1, 1) nuclear peak was $R = \frac{\mathrm{NSF}_N}{\mathrm{SF}_N} \approx \frac{20{,}040}{650} \approx 30.8$ for experiments on sample 1. The flipping ratio was ~38 for sample 2. Scan at each point/energy takes ~35 s for NSF channels and ~175 s for SF channels. Due to the low incident neutron energies, no neutron filter was used.

The x, y and z neutron polarization directions are defined as parallel to $\mathbf{Q}$, perpendicular to $\mathbf{Q}$ but in the scattering plane, and perpendicular to $\mathbf{Q}$ and the scattering plane, respectively (Fig. 1c). The corresponding NSF and SF neutron scattering cross-sections are summarized in equation (3). For polarized neutron scattering (elastic or inelastic) experiments with only vertical (z-axis) neutron polarization, the SF and NSF neutron scattering cross-sections are $\sigma_z^{\mathrm{SF}} = \frac{R}{R+1}M_y + \frac{1}{R+1}(M_z + N) + \frac{1}{R+1}[\frac{(2R+1)}{3}\mathrm{NSI} + (R+1)B]$ and $\sigma_z^{\mathrm{NSF}} = \frac{1}{R+1}M_y + \frac{R}{R+1}(M_z + N) + \frac{1}{R+1}[\frac{(R+2)}{3}\mathrm{NSI} + (R+1)B]$, respectively.

Using full neutron polarization analysis by measuring $\sigma_{x,y,z}^{\mathrm{SF}}(\mathbf{Q}, E)$ and $\sigma_x^{\mathrm{NSF}}(\mathbf{Q}, E)$ at accessible values of $\mathbf{Q}$ and E, one can determine M_y and M_z, without the need to change the temperature. In particular, M_y and M_z can be solely determined from $\sigma_{x,y,z}^{\mathrm{SF}}(\mathbf{Q}, E)$ using the first three rows of equation (3), which is exact for a paramagnet like $Ce_2Zr_2O_7$. We have

$$\sigma_x^{\mathrm{SF}} = \frac{R}{R+1}M_y + \frac{R}{R+1}M_z + C_1, \tag{4}$$

$$\sigma_y^{\mathrm{SF}} = \frac{1}{R+1}M_y + \frac{R}{R+1}M_z + C_1, \tag{5}$$

$$\sigma_z^{\mathrm{SF}} = \frac{R}{R+1}M_y + \frac{1}{R+1}M_z + C_1, \tag{6}$$

where $C_1 = \frac{1}{R+1}N + \frac{(2R+1)/3}{R+1}\mathrm{NSI} + B$;

$$\text{Equation (4)} - \text{Equation (5)}\ \text{gives}\ M_z = \frac{R+1}{R-1}\left(\sigma_x^{\mathrm{SF}} - \sigma_z^{\mathrm{SF}}\right); \tag{7}$$

$$\text{Equation (4)} - \text{Equation (6)}\ \text{gives}\ M_y = \frac{R+1}{R-1}\left(\sigma_x^{\mathrm{SF}} - \sigma_y^{\mathrm{SF}}\right); \tag{8}$$

$$\text{Equation (7)} + \text{Equation (8)}\ \text{gives}\ M_y + M_z = \frac{R+1}{R-1}\left(2\sigma_x^{\mathrm{SF}} - \sigma_y^{\mathrm{SF}} - \sigma_z^{\mathrm{SF}}\right); \tag{9}$$

$$\text{Equation (7)} - \text{Equation (8)}\ \text{gives}\ M_z - M_y = \frac{R+1}{R-1}\left(\sigma_y^{\mathrm{SF}} - \sigma_z^{\mathrm{SF}}\right). \tag{10}$$

The flipping ratio, $R \approx 30$, is a typical value from experience on ThALES. In principle, there is an uncertainty of R of a few per cents, but in our case, this would have a very small effect. A 10% uncertainty of R (from 30 to 27) would give a 0.6% uncertainty of $\frac{R+1}{R-1}$ (from 1.069 to 1.077) M_y or M_z. A 50% uncertainty of R (from 30 to 15) would only give a 7% uncertainty of $\frac{R+1}{R-1}$ (from 1.069 to 1.142) M_y or M_z. For this reason, we can safely ignore the uncertainties of R.

Using the last three rows of equation (3), we can also extract M_y and M_z from $\sigma_{x,y,z}^{\mathrm{NSF}}(\mathbf{Q}, E)$:

$$\sigma_x^{\mathrm{NSF}} = \frac{1}{R+1}M_y + \frac{1}{R+1}M_z + C_2, \tag{11}$$

$$\sigma_y^{\mathrm{NSF}} = \frac{R}{R+1}M_y + \frac{1}{R+1}M_z + C_2, \tag{12}$$

$$\sigma_z^{\mathrm{NSF}} = \frac{1}{R+1}M_y + \frac{R}{R+1}M_z + C_2, \tag{13}$$

where $C_2 = \frac{R}{R+1}N + \frac{(R+2)/3}{R+1}\mathrm{NSI} + B$;

$$\text{Equation (12)} - \text{Equation (11)}\ \text{gives}\ M_y = \frac{R+1}{R-1}\left(\sigma_y^{\mathrm{NSF}} - \sigma_x^{\mathrm{NSF}}\right); \tag{14}$$

$$\text{Equation (13)} - \text{Equation (11)}\ \text{gives}\ M_z = \frac{R+1}{R-1}\left(\sigma_z^{\mathrm{NSF}} - \sigma_x^{\mathrm{NSF}}\right); \tag{15}$$

$$\text{Equation (14)} + \text{Equation (15)}\ \text{gives}\ M_y + M_z = \frac{R+1}{R-1}\left(-2\sigma_x^{\mathrm{NSF}} + \sigma_y^{\mathrm{NSF}} + \sigma_z^{\mathrm{NSF}}\right); \tag{16}$$

$$\text{Equation (15)} - \text{Equation (14)}\ \text{gives}\ M_z - M_y = \frac{R+1}{R-1}\left(\sigma_z^{\mathrm{NSF}} - \sigma_y^{\mathrm{NSF}}\right). \tag{17}$$

However, $\sigma_{x,y,z}^{\mathrm{NSF}}(\mathbf{Q}, E)$ contains nuclear scattering (N), which is much larger than NSI, especially at the elastic line. Therefore, we will have much larger uncertainties in obtaining the values of M_y and M_z due to the propagation of statistical errors (Supplementary Table 2). In practice, one would not use $\sigma_{x,y,z}^{\mathrm{NSF}}(\mathbf{Q}, E)$ to extract the magnetic signal. Also, our counting time for $\sigma_{x,y,z}^{\mathrm{NSF}}(\mathbf{Q}, E)$ is only one-fifth that of $\sigma_{x,y,z}^{\mathrm{SF}}(\mathbf{Q}, E)$, resulting in even larger errors when calculating M_y and M_z.

To estimate the instrumental energy resolution, we fit the energy scans of σ_x^{NSF} at different $\mathbf{Q}$ values (Extended Data Fig. 2). For $E_f = 3.23$ meV, the instrumental energy resolution is about 0.065 meV at the FHWM. For $E_f = 2.52$ meV, the energy resolution is 0.042 meV at the FHWM. For our measurements on sample 2 with $E_f = 2.52$ meV and $E_f = 3.23$ meV at (0, 0, 1), the instrumental energy resolutions are 0.035 meV and 0.052 meV, respectively (Extended Data Fig. 2d,e). Extended Data Fig. 3 compares the raw data of $\sigma_x^{\mathrm{NSF}}(\mathbf{Q})$ with $\sigma_{x,y,z}^{\mathrm{SF}}(\mathbf{Q})$ at the elastic position $E = 0 \pm 0.03$ meV. We see that NSF scattering dominates the scattering signal at all the probed $\mathbf{Q}$ values. Extended Data Fig. 3g,h compares the raw data of $\sigma_x^{\mathrm{NSF}}(\mathbf{Q})$ with $\sigma_{x,y,z}^{\mathrm{SF}}(\mathbf{Q})$ at the inelastic position $E = 0.1 \pm 0.03$ meV. Here magnetic scattering in the SF channel is larger than non-magnetic scattering in the NSF channel.

To compare our measurements discussed in Figs. 1–4 with the energy-integrated spin–spin correlation function $S^y(\mathbf{Q}) = \int M_y(\mathbf{Q}, E)\mathrm{d}E$ and $S^z(\mathbf{Q}) = \int M_z(\mathbf{Q}, E)\mathrm{d}E$ discussed before[42], we integrated $M_y(\mathbf{Q}, E)$ and $M_z(\mathbf{Q}, E)$ (Fig. 2) in energy at the X and K points and compare the outcome with our theoretical model and ref. 42 in Supplementary Table 1.

From Supplementary Table 1, we see that our estimated $\int M_z(E)\mathrm{d}E$ is about 50% smaller than that from $\sigma_z^{\mathrm{NSF}}(\mathbf{Q})$ measurements[42]. From equation (3), we note that $\sigma_z^{\mathrm{NSF}}(\mathbf{Q})$ is sensitive to nuclear scattering (including phonons, N) in addition to the usual background scattering (B). To understand the problem, we note all previous unpolarized[38,39] and vertical field-polarized[42] neutron scattering experiments assume

that the background and other non-magnetic scattering is temperature independent between the base and high temperatures. Using our measured $\sigma^{SF}_{x,y,z}(\mathbf{Q},E)$ and $\sigma^{NSF}_{x}(\mathbf{Q},E)$ values, we can determine N, NSI and B at the elastic position at base temperature (50 mK) without the need for high-temperature data. At $\mathbf{Q}=(0,0,1)$ and $E=0\pm0.03$ meV, we find $C_1=\frac{1}{R+1}N+\frac{(2R+1)/3}{R+1}\mathrm{NSI}+B=326$, $C_2=\frac{R}{R+1}N+\frac{(R+2)/3}{R+1}\mathrm{NSI}+B=603$, $M_y=57.5$ and $M_z=62$ (Supplementary Table 2). As NSI scattering is typically fairly small, nuclear scattering in the NSF channel is comparable with the background scattering. Therefore, $\sigma^{NSF}_{z}(\mathbf{Q})$ measurements contain considerable nuclear scattering that needs to be eliminated, and the intrinsic magnetic signal is about 10% of non-magnetic scattering.

To improve the statistics and compare with theoretical calculations, we repeated the measurements of $\sigma^{SF}_{x,y,z}(\mathbf{Q},E)$ and $\sigma^{NSF}_{x,y,z}(\mathbf{Q},E)$ almost 3–5 times at $\mathbf{Q}=(0,0,1)$, $(1,1,0)$, $(0.5,0.5,0.5)$, $(0,0,2)$ and $(0,0,3)$ (Figs. 1b and 3a) with $E=0\pm0.03$ meV and $E=0.1\pm0.03$ meV. This allows an overall determination of M_y and M_z. Supplementary Table 2 summarizes these results at the elastic position and our calculation of M_y+M_z, M_y and M_z. Supplementary Table 3 compares the outcome with the theoretical calculations. Supplementary Tables 4 and 5 summarize similar results at $E=0.1\pm0.03$ meV. Overall, these results are consistent with those discussed in Figs. 2–4.

Problems with using high-temperature (~10 K) as background in unpolarized neutron scattering experiments

In our previous unpolarized neutron scattering experiment[39], we assumed that the magnetic scattering at 12 K is diffusive enough and would be $\mathbf{Q}$ and E independent and can, thus, serve as the non-magnetic background. However, the Bose population factor dictates that any bosonic excitations (acoustic phonons and other background scattering) within 1 meV would be populated at 12 K and suppressed at 50 mK (Extended Data Fig. 4a,b). This is especially important at elastic and quasielastic positions for $Ce_2Zr_2O_7$, where N and B have about 90% of the total scattering signal. From comparing the integrated intensity along the $[0,0,l]$ and $[h,h,0]$ directions at the elastic line at 35 mK and 12 K (Extended Data Fig. 4c,d), we clearly see that the intensity at 12 K is higher than that at 35 mK in most of the reciprocal space in the scattering plane, probably due to thermally induced quasielastic scattering at 12 K. Therefore, magnetic excitations at energies near zero were overlooked by the incorrect oversubtraction in unpolarized neutron scattering experiments. Even for polarized neutron scattering experiments with only vertical neutron polarization[42], high-temperature measurements were used as background scattering and similar problems may occur. For CSI such as $Ho_2Ti_2O_7$ with a large effective magnetic moment, the magnetic scattering is many times larger than that of $Ce_2Zr_2O_7$ (refs. 22–24,38,39). Therefore, a polarized neutron scattering experiment with only vertical neutron polarization using $\sigma^{SF}_{z}(\mathbf{Q})$ and $\sigma^{NSF}_{z}(\mathbf{Q})$ can still accurately determine M_y and M_z due to the overwhelming magnetic signal compared with the magnitudes of N, NSI and B scattering[24]. This is incorrect for $Ce_2Zr_2O_7$ with effective $S=1/2$ (Figs. 2 and 3 and Supplementary Table 2).

Possible effect of chemical disorder

As determined from an earlier work[39], there is a 4% antisite disorder of Ce and Zr from X-ray diffraction. Though $Ce_2Zr_2O_7$ can be air sensitive, our single-crystal samples were stored in an Ar glovebox before and after the experiments, and we found no evidence of oxidation. Our data for $Ce_2Zr_2O_7$ are consistent with the INS data of the $Ce_2Sn_2O_7$ powder sample for energies above 0.03 meV, which has less disorder[56]. Recent work on single crystals of $Ce_2Sn_2O_7$ (ref. 45), which has about 3% B-site stuffing of Ce^{4+} (comparable with 4% in $Ce_2Zr_2O_7$), behave similar to $Ce_2Sn_2O_7$ powder in terms of heat capacity and other properties. From this perspective, a few per-cent disorder in $Ce_2Zr_2O_7$ should not induce the wavevector-dependent scattering (Fig. 3e) and spin excitations should not be anisotropic in the spin space (Fig. 3c).

Disorder can play a significant role in modifying the magnetic behaviour, and there are examples in which even small amounts can lead to notable changes. In the case of the non-Kramers doublet system of $Pr_2Zr_2O_7$, disorder lifts the degeneracy of the doublet, leading to a broadened spin excitation spectrum centred at around 0.4 meV (refs. 36,64). However, in $Ce_2Zr_2O_7$, the robustness of the Kramers doublet ground state makes it less sensitive to this type of perturbation. Moreover, there are Kramers doublet systems that exhibit sensitivity to disorder. For instance, $Yb_2Ti_2O_7$, which lies near the phase boundary between a canted ferromagnetic phase and a Γ_5 antiferromagnetic phase, demonstrates that disorder can destabilize one phase and favour another. Local variations in exchange interactions due to disorder can shift the balance between ferromagnetic, antiferromagnetic or spin-liquid-like behaviours[37]. By contrast, $Ce_2Zr_2O_7$ is not known to be near such phase boundaries, and no changes in magnetic phases have been reported due to disorder in Ce-based pyrochlores, including $Ce_2T_2O_7$ (T = Zr, Sn or Hf).

Moreover, a.c. susceptibility measurements in $Ce_2T_2O_7$ show no frequency dependence, indicating that the observed disorder is unlikely to induce a spin-glass state[38–45]. Although complete B-site disorder in Ce_2NbSbO_7 has been shown to result in a spin-glass behaviour (evidenced by clear peaks and frequency dependence in a.c. susceptibility measurements in our unpublished work), the 4% disorder observed in $Ce_2T_2O_7$ appears insufficient to cause such an effect.

The large temperature gradient during the floating-zone growth process probably contributes to the observed 4% disorder in $Ce_2T_2O_7$. Future advancements in synthesis techniques or annealing methods may help reduce the level of disorder, though its complete elimination is unlikely. The amount of disorder necessary to disrupt the prospective realization of QSI in dipolar–octupolar remains an open issue. Our work, thus, calls for systematic investigations of the role of disorder in Ce-based spin-ice compounds.

Is the signal inelastic or elastic?

From both muon spin spectroscopy and heat capacity measurements, there is no evidence of magnetic order down to 20 mK, indicating that the observed scattering cannot originate from excitations tied to magnetic ordering[39,55]. Additionally, earlier neutron diffuse scattering studies found no vacancy-induced diffuse scattering across the energy ranges studied[53,54]. These observations suggest that the signal is magnetic in origin but not related to long-range order.

Unlike the gapped spinon excitations observed in some QSL candidates, the signal attributed to emergent photons in $Ce_2T_2O_7$ is gapless and lies very close to the elastic line. From the heat capacity data, the T^3 scaling persists up to approximately 60 mK, corresponding to an energy of about 0.005 meV. However, this energy range is much smaller than the experimental resolution (0.035–0.076 meV), making it challenging to clearly resolve this signal from the elastic line. Although the presence of gapless excitations is consistent with emergent photons in the $U(1)$ QSL framework, the overlap with elastic scattering requires careful analysis to distinguish these features confidently.

To investigate further, we fit the magnetic signal near the elastic line to determine relative shifts compared with the elastic signal. As shown in Fig. 2n, the data perhaps hint at a small shift, although it is well within the energy resolution. Similar shifts were fitted for the magnetic signals in M_y+M_z (Fig. 2d–f), M_y and M_z. Below are the fitted centre positions with uncertainties from Extended Data Figs. 6–8.

- At $\mathbf{Q}=(0,0,1)$:
- $C(M_y)=0.03143\pm0.0074$ meV,
- $C(M_z)=0.03104\pm0.00773$ meV,
- $C(M_y+M_z)=0.03079\pm0.00688$ meV.

- At $\mathbf{Q} = (3/4, 3/4, 0)$:
- $C(M_y) = (8.97 \pm 7.29) \times 10^{-4}$ meV,
- $C(M_z) = (1.69 \pm 0.555) \times 10^{-3}$ meV,
- $C(M_y + M_z) = (9.33 \pm 6.68) \times 10^{-4}$ meV.
- At $\mathbf{Q} = (1, 1, 0)$:
- $C(M_y) = 0.00569 \pm 0.00367$ meV,
- $C(M_z) = 0.00924 \pm 0.0056$ meV,
- $C(M_y + M_z) = 0.0796 \pm 0.00418$ meV.

Among the three $\mathbf{Q}$ points, the scans at $\mathbf{Q} = (0, 0, 1)$ provide the best statistics due to extended scan times, although at the expense of poorer energy resolution. Conversely, scans at $\mathbf{Q} = (1, 1, 0)$ achieve a higher energy resolution, whereas those at $\mathbf{Q} = (3/4, 3/4, 0)$ are limited by both resolution and fewer scan repetitions. Nevertheless, none of the scans exhibit shifts in the magnetic signal into the $E < 0$ regime, even within the resolution limits.

In ideal circumstances, one could achieve higher energy resolution by reducing the incident neutron energy (E_i) to better isolate the magnetic signal near the elastic line. However, practical limitations such as beamtime and instrument flux impose constraints. The best experimental setup used here achieves a resolution of 0.035 meV (corresponding to $E_i = 2.52$ meV) on a cold neutron spectrometer, either at a triple-axis spectrometer like ThALES or a time-of-flight (TOF) instrument like the Cold Neutron Chopper Spectrometer at the Spallation Neutron Source. Unpolarized TOF neutron scattering struggles to detect pure magnetic signals near the elastic line due to background subtraction challenges, whereas a polarized triple-axis spectrometer provides greater precision at the cost of reduced flux, approximately 10^{-4}–10^{-5} that of unpolarized TOF. For comparison, acquiring sufficient statistics in a polarized triple-axis spectrometer would require ~138 days, compared with ~20 min for a single TOF scan for one angle, rendering this approach impractical.

In conclusion, although the observed scattering near the elastic line is consistent with gapless magnetic excitations, the limitations of experimental resolution complicate distinguishing these signals. Further studies with optimized setups and analysis are required to definitively isolate and characterize these excitations.

Correlation lengths of the inelastic and quasielastic excitations

Fitting of the inelastic scattering signals along the (0, 0, l) direction (Extended Data Fig. 4f) yields an FWHM $\sigma_k = 1.1446 \pm 0.2824$ and associated correlation length (CL) $= \frac{\sqrt{2\ln 2}a_0}{\pi\sigma_k} = 3.504 \pm 1.147$ Å. Proceeding similarly for the quasielastic scattering signals (Fig. 2g) yields FWHM $\sigma_k = 0.8245 \pm 0.5121$ and the resulting CL $= \frac{\sqrt{2\ln 2}a_0}{\pi\sigma_k} = 4.87 \pm 3.01$ Å. These results suggest that the inelastic and quasielastic excitations have similar correlation lengths and, therefore, arise from the same crystalline lattice of $Ce_2Zr_2O_7$. It is difficult to imagine that a small disorder in $Ce_2Zr_2O_7$ can give rise to dominant magnetic scattering signals at the quasielastic positions that have similar correlation lengths as higher-energy excitations.

Theoretical calculation of the dynamical spin structure factor in π-D-QSI

Considering that we are interested in a small momentum transfer, we assume that the octupolar magnetic form factor associated with the τ^x and τ^y moments can be neglected and that the magnetic form factor of τ^z is constant over the momentum transfers of interest. Then, the magnetic scattering along the local y and z axes has the generic form

$$M^{y(z)}(\mathbf{Q}, E) = \frac{C}{N_{\text{u.c.}}} \int \mathrm{d}t \sum_{i,j} P_{ij}^{y(z)}(\mathbf{Q})\, \mathrm{e}^{\mathrm{i}(Et + \mathbf{Q}\cdot(\mathbf{R}_i - \mathbf{R}_j))} \left\langle \tau_i^z(t)\, \tau_j^z(0) \right\rangle, \quad (18)$$

where C is a global prefactor that depends on the parameters of the experiment under consideration (for example, sample size and neutron flux); $\mathbf{R}_i$ labels the position of site i; and $P_{ij}(\mathbf{Q})$ is a polarization factor that depends on the sublattices of sites i and j, the momentum transfer $\mathbf{Q}$ and the direction of magnetic scattering. Specifically, for M_z and M_y, we have $P^z{}_{ij}(\mathbf{Q}) = (\hat{\mathbf{e}}_{i,z} \cdot \hat{\mathbf{z}}_{\text{sc}})(\hat{\mathbf{e}}_{j,z} \cdot \hat{\mathbf{z}}_{\text{sc}})$ and $P^y{}_{ij}(\mathbf{Q}) = (\hat{\mathbf{e}}_{i,z} \cdot \frac{\mathbf{Q}\times\hat{\mathbf{z}}_{\text{sc}}}{|\mathbf{Q}\times\hat{\mathbf{z}}_{\text{sc}}|})(\hat{\mathbf{e}}_{j,z} \cdot \frac{\mathbf{Q}\times\hat{\mathbf{z}}_{\text{sc}}}{|\mathbf{Q}\times\hat{\mathbf{z}}_{\text{sc}}|})$, respectively, where $\hat{\mathbf{z}}_{\text{sc}}$ is a unit vector perpendicular to the scattering plane and $\hat{\mathbf{e}}_{i,z}$ are the basis vectors along the local z axis for the pseudospin frame at site i. Using the pseudospins in the XYZ model, the above expression can be rewritten as

$$M^{y(z)}(\mathbf{Q}, E) = \frac{C}{N_{\text{u.c.}}} \int \mathrm{d}t \sum_{i,j} P_{ij}^{y(z)}(\mathbf{Q})\, \mathrm{e}^{\mathrm{i}(Et + \mathbf{Q}\cdot(\mathbf{R}_i - \mathbf{R}_j))} \left(\cos^2\theta \left\langle S_i^z(t)\, S_j^z(0) \right\rangle + \sin^2\theta \left\langle S_i^x(t)\, S_j^x(0) \right\rangle \right). \quad (19)$$

With the slave–particle construction introduced in the main text, the dynamical averages for π-D-QSI become $\left\langle S_i^x S_j^x \right\rangle = \left\langle \mathscr{E}_{r_1,r_2} \mathscr{E}_{r_3,r_4} \right\rangle$, which gives the photon propagator. Here r_1, r_2, r_3 and r_4 label the centres of the tetrahedra such that r_1 and r_3 (r_2 and r_4) correspond to up (down) tetrahedra, and i and j sit at the middle of the bond $r_1 \to r_2$ and $r_3 \to r_4$, respectively. For the transverse correlation, we first rewrite the expression in terms of raising/lowering operators as $\langle S_i^z S_j^z \rangle = -\frac{1}{4}(\langle S_i^+ S_j^+ \rangle - \langle S_i^- S_j^+ \rangle - \langle S_i^+ S_j^- \rangle + \langle S_i^- S_j^- \rangle)$ before rewriting everything with spinon operators

$$\left\langle S_i^z S_j^z \right\rangle = -\frac{1}{16} \left(\left\langle \Phi_{r_1}^\dagger \mathrm{e}^{\mathrm{i}\mathscr{A}_{r_1,r_2}} \Phi_{r_2} \Phi_{r_3}^\dagger \mathrm{e}^{\mathrm{i}\mathscr{A}_{r_3,r_4}} \Phi_{r_4} \right\rangle - \left\langle \Phi_{r_2}^\dagger \mathrm{e}^{-\mathrm{i}\mathscr{A}_{r_1,r_2}} \Phi_{r_1} \Phi_{r_3}^\dagger \mathrm{e}^{\mathrm{i}\mathscr{A}_{r_3,r_4}} \Phi_{r_4} \right\rangle - \left\langle \Phi_{r_1}^\dagger \mathrm{e}^{\mathrm{i}\mathscr{A}_{r_1,r_2}} \Phi_{r_2} \Phi_{r_4}^\dagger \mathrm{e}^{-\mathrm{i}\mathscr{A}_{r_3,r_4}} \Phi_{r_3} \right\rangle + \left\langle \Phi_{r_2}^\dagger \mathrm{e}^{-\mathrm{i}\mathscr{A}_{r_1,r_2}} \Phi_{r_1} \Phi_{r_4}^\dagger \mathrm{e}^{-\mathrm{i}\mathscr{A}_{r_3,r_4}} \Phi_{r_3} \right\rangle \right). \quad (20)$$

In the following subsections, we explain how to evaluate the electric-field propagator using Gaussian quantum electrodynamics and the four spinon correlations using GMFT.

GMFT

To use GMFT, we first rewrite the XYZ model in terms of raising/lowering spin operators as

$$\mathscr{H} = \sum_{\langle i,j \rangle} \left[\mathcal{J}_{\parallel} S_i^{\parallel} S_j^{\parallel} - \mathcal{J}_{\pm} \left(S_i^+ S_j^- + S_i^- S_j^+ \right) + \mathcal{J}_{\pm\pm} \left(S_i^+ S_j^+ + S_i^- S_j^- \right) \right], \quad (21)$$

where, for π-D-QSI, $\mathcal{J}_{\parallel} = \mathcal{J}_x$, $\mathcal{J}_{\pm} = -(\mathcal{J}_z + \mathcal{J}_y)/4$ and $\mathcal{J}_{\pm\pm} = (\mathcal{J}_y - \mathcal{J}_z)/4$. In GMFT, the initial spin-1/2 Hilbert space on the pyrochlore lattice is augmented to a new, larger one for which the bosonic degrees of freedom are introduced on the parent (premedial) diamond lattice whose sites are centred on the initial tetrahedra. For this mapping to be exact, the discretized Gauss's law $Q_r = \eta_r \sum_{i \in r} S_i^{\parallel}$ needs to be imposed on all the tetrahedra, where the sum is over all 4 sites that are part of the tetrahedra and $\eta_r = +1$ (-1) if r is an up (down) tetrahedron. After mapping the pseudospin component with the dominant coupling to the emergent electric field $S_i^{\parallel} = \mathscr{E}_{r,r'}$, the above definition is interpreted as a lattice divergence (that is, $\mathbf{Q} = \nabla \cdot \mathscr{E}$). The boson raising and lowering operators can then be defined as $\Phi_r^\dagger = \mathrm{e}^{\mathrm{i}\phi_r}$ and $\Phi_r = \mathrm{e}^{-\mathrm{i}\phi_r}$, respectively, where ϕ_r is canonically conjugate to Q_r. These quantum rotors respect $|\Phi_r^\dagger \Phi_r| = 1$ by construction. Using the mapping $S_i^+ = \frac{1}{2}\Phi_r^\dagger \mathrm{e}^{\mathrm{i}\eta_r \mathscr{A}_{r,r'}} \Phi_{r'}$ and $S_i^{\parallel} = \mathscr{E}_{r,r'}$ introduced in the main text, the Hamiltonian can be rewritten as an interacting quantum rotor model strongly coupled to a compact $U(1)$ gauge field. The interpretation of the above construction

is that $S^{\parallel}$ corresponds to the emergent electric field, which is divergence-less (that is, $\nabla \cdot \mathscr{E} = 0$) in the two-in–two-out manifold (that is, when $\mathcal{J}_{\parallel}$ is much larger than the other couplings). Flipping this lattice field with $e^{i\mathscr{A}_{r,r'}}$ breaks the ice rules (that is, $\nabla \cdot \mathscr{E} \neq 0$) and must then be accompanied by the creation of a spinon–antispinon pair (Fig. 1e) that act as sources of the emergent field.

To get a tractable model, we carry out three successive approximations. (1) The four boson interactions coming from the $U(1)$ symmetry-breaking term $\mathcal{J}_{\pm\pm}$ are decoupled as $\Phi_i^\dagger\Phi_i^\dagger\Phi_j\Phi_k \to \Phi_i^\dagger\Phi_i^\dagger\chi_{j,k} + \Phi_j\Phi_k\left(\chi_{i,i}^0\right)^* + 2\Phi_i^\dagger\Phi_j\xi_{i,k} + 2\Phi_i^\dagger\Phi_k\xi_{i,j}$, where χ, χ^0 and ξ are mean-field parameters representing intersite pairing, on-site pairing and intersublattice hopping, respectively. (2) The bosonic matter and dynamical gauge field sectors are decoupled by fixing the gauge field to a constant background $\mathscr{A} \to \bar{\mathscr{A}}$, where we pick a gauge configuration such that $\nabla \times \bar{\mathscr{A}} = \pi$ in the π-flux QSI phase and $\nabla \times \bar{\mathscr{A}} = 0$ in the 0-flux phase. (3) We relax the constraint $|\Phi_r^\dagger\Phi_r| = 1$ to the average one ($\langle\Phi_r^\dagger\Phi_r\rangle = \kappa$) by performing a large-$N$ approximation. $\langle A\rangle$ denotes a thermal average, and the constraint is imposed by tuning a Lagrange multiplier λ. Here $\kappa = 2$ is chosen since such a constraint recovers the correct spinon dispersion in the Ising limit and agrees with quantum Monte Carlo (QMC) results for the position of the phase transition from the 0-flux QSI to an ordered state[51,52]. Such a choice also agrees with QMC and exact diagonalization (ED) for the position of the lower and upper edges of the two-spinon continuum for 0-flux and π-flux QSI[52]. It should be emphasized that despite the apparent severity of such approximations, GMFT has been extensively benchmarked and shown to give worthwhile qualitative agreement with state-of-the-art QMC, ED and pseudofermions functional renormalization group[52]. After such approximations, we have a non-interacting quadratic Hamiltonian that can be diagonalized exactly. When solving the self-consistency conditions in the relevant parameter regimes, it is found that all the mean-field parameters vanish in the deconfined phase ($\chi = 0, \xi = 0$ and $\chi^0 = 0$). GMFT is, thus, insensitive to $\mathcal{J}_{\pm\pm}$ for the parameter regime of interest. Consequently, only $\mathcal{J}_{\parallel}$ and $\mathcal{J}_{\pm}$ are fitted when comparing with experiments. From this quadratic Hamiltonian, the dynamical spin structure factor can be evaluated as that in ref. 52. We emphasize that in our modelling, the spinons and photons are effectively decoupled such that the spinons are only sensitive to the average background π-flux threading the hexagonal plaquettes.

Gaussian quantum electrodynamics

The low-energy physics of the spin-ice manifold can be described by a compact $U(1)$ gauge theory

$$\mathscr{H}_{\mathcal{U}(1)} = \frac{\mathcal{U}}{2}\sum_{\langle r,r'\rangle}\mathscr{E}_{r,r'}^2 - \mathcal{K}\sum_{\mathrm{h}}\cos\left(\nabla\times\mathscr{A}\right)_{\mathrm{h}}, \tag{22}$$

where the second sum is over hexagonal plaquettes. In its deconfined phase (that is, for QSI), the low-energy physics of a compact $U(1)$ gauge theory can be approximated by

$$\mathscr{H}_{\mathcal{U}(1)} \approx \frac{\mathcal{U}}{2}\sum_{\langle r,r'\rangle}\mathscr{E}_{r,r'}^2 + \frac{\mathcal{K}}{2}\sum_{\mathrm{h}}\left(\nabla\times\mathscr{A}\right)_{\mathrm{h}}^2. \tag{23}$$

This quadratic Hamiltonian can be diagonalized to compute the dynamical spin structure factor at a finite temperature due to photons, as explained in ref. 30. This procedure yields

$$\begin{aligned}&\int \mathrm{d}t\sum_{i,j} e^{i(Et+\mathbf{Q}\cdot(\mathbf{R}_i-\mathbf{R}_j))}\left\langle\mathscr{E}_{r_1,r_2}(t)\,\mathscr{E}_{r_3,r_4}(0)\right\rangle\\ &= \frac{\zeta^2\mathcal{K}}{2E(\mathbf{Q})}\sum_{\mu}\sum_{\lambda}\sin\left(\mathbf{Q}\cdot h_{\mu\nu}\right)\sin\left(\mathbf{Q}\cdot h_{\nu\lambda}\right)\left[n_{\mathrm{B}}\left(E(\mathbf{Q})\right)\delta\left(E+E(\mathbf{Q})\right)\right.\\ &\left.+\left(1+n_{\mathrm{B}}\left(E(\mathbf{Q})\right)\right)\delta\left(E-E(\mathbf{Q})\right)\right].\end{aligned} \tag{24}$$

$\mu, \nu, \lambda \in \{0, 1, 2, 3\}$ label the four pyrochlore sublattices, $h_{\mu\nu} = a_0\left(b_\mu \times b_\nu\right)/\left(\sqrt{8}\,|b_\mu \times b_\nu|\right)$, where b_μ are the vectors connecting an up tetrahedron to its four nearest-neighbour down tetrahedra, n_{B} is the Bose–Einstein distribution and $E(\mathbf{Q})$ is the photon dispersion. ζ is a dimensionless parameter that is meant to take into account any renormalization of the electric field when integrating high-energy degrees of freedom to derive the above effective field theory. We set $\zeta = 1$. Any other choice would affect the relative intensity of the photon and spinon contributions and the fitted θ value.

The parameters $\mathcal{U}$ and $\mathcal{K}$ are related to the speed of the emergent light by $c_{\mathrm{QSI}} = \sqrt{\mathcal{U}\mathcal{K}}\,a_0\hbar^{-1}$. The speed of light fully determines the photon dispersion in this description, but the intensity of the dynamical spin structure factor depends on the specific ratio of $\mathcal{U}$ and $\mathcal{K}$ (ref. 30). Both $\mathcal{U}$ and $\mathcal{K}$, thus, need to be fixed. In the perturbative regime close to the Ising point, one can relate $\mathcal{K}$ to the perturbative ring exchange term obtained by going to the third order in perturbation theory (that is, $\mathcal{K} \propto \mathcal{J}_{\pm}^3/\mathcal{J}_{\parallel}^2$) and fix $\mathcal{U}$ by using previous QMC results[30]. However, since we are far from this perturbative regime, we make no such assumption regarding possible connections between parameters of the effective theory and the microscopic couplings of the initial spin Hamiltonian. Instead, we fix c_{QSI} and then use the results of ref. 32, where the effective ring exchange model of equation (23) was studied using large-scale ED simulations. This investigation reports that $\hbar c_{\mathrm{QSI}}/a_0 = 0.51(6)\,\mathcal{K}/2$. We, thus, use these results to fix $\mathcal{U}$ and $\mathcal{K}$ given c_{QSI}.

Exploration of alternative explanations for the quasielastic signal

Thermal spinons. Within GMFT, spinons can also produce a quasielastic signal at finite temperatures. Indeed, at finite temperatures, instead of exciting two spinons, a neutron can be scattered by de-exciting a thermally excited spinon and exciting another one from the vacuum for a net approximately null energy transfer. However, we find that this quasielastic signal from thermal spinons is systematically much smaller than the inelastic contribution for the experimental temperature of $T = 50$ mK and $T = 33$ mK (Fig. 1d). It, thus, appears implausible that thermal spinons could yield the dominant quasielastic signal we report.

A broader spinon continuum. A natural question is whether one can fit the whole signal by simply lowering the spinon gap without invoking the emergent photon. It should first be noted that in a deconfined phase (that is, QSI), the bosonic spinons need to have a finite gap Δ_{spinon}. A gapless bosonic spinon dispersion would lead to spinon condensation and, thus, indicate a transition to a magnetically long-range ordered state. INS probes the two-spinon continuum. As such, it is only non-zero for energies above the lower edge of the two-spinon continuum $2\Delta_{\mathrm{spinon}}$ (in the non-interacting limit). Suppose only the spinons contribute to the dynamical spin structure factor. In that case, we only expect an inelastic signal for which quasielastic contribution would come from the leaking of the inelastic contribution due to finite energy resolution (and the small contribution from the thermal spinons mentioned above). Provided the energy step size in the signal measured is sufficiently small compared with the gap, the signal's maximum should then necessarily be for a non-zero energy transfer. This already seems at odds with our measurements, where we systematically see the maximum of the total magnetic signal $M_z + M_y$ at (or very close to) the elastic line for the three momentum transfers reported in Fig. 2.

Before exploring further, it should also be emphasized that we believe GMFT to yield reasonable estimates for the position of the two-spinon continuum. Indeed, it gives good agreement for the position of the continuum with the QMC results in ref. 28 for 0-QSI and the 32-site ED results in ref. 50 for π-QSI (Extended Data Fig. 5). The microscopic exchange couplings of $Ce_2Zr_2O_7$ have already been estimated through a detailed examination of thermodynamics and neutron scattering measurements[42,49]. The GMFT prediction for the spinon contribution to the dynamical spin structure factor using these parameters

yields a first peak at approximately 0.05 meV and a second one at around 0.1 meV (ref. 52). This is in agreement with our measurements and interpretation of the energy scans shown in Fig. 2. Considering both agreement for the predicted spinon gap of GMFT, ED and QMC and the parameter sets that have been put forward through careful analysis of thermodynamic measurements, a spinon peak at much lower energies is unlikely. A much lower spinon peak would probably yield predictions incompatible with the system's thermodynamic behaviour.

Nonetheless, we still tried to see if the results could be fitted by a spinon signal with a smaller gap without invoking any supplemental quasielastic contribution. To this end, we can reduce the position of the spinon peak by increasing $\mathcal{J}_\pm/\mathcal{J}_\parallel$ and decreasing $\mathcal{J}_\parallel$ (Extended Data Fig. 6). In particular, using $\mathcal{J}_\parallel = 0.06$ meV and $\mathcal{J}_\pm/\mathcal{J}_\parallel = -0.35$ produces a signal for which the first spinon peak is at around 0.03 meV (Extended Data Fig. 7). Such a spinon signal systematically fails to capture the large contribution at the elastic line. This is especially apparent when looking at the residual, in which we clearly see a large signal missed at the elastic line. This residual can be accounted for using a Gaussian function centred at around $E \approx 0$ meV with a width comparable to the experimental resolution. This is highly suggestive that there is an additional mode near zero energy regardless of any other consideration.

In short, it does not seem probable that our measurements can be accounted for using a spinon signal with a much smaller gap because this would probably be incompatible with the previously established thermodynamic behaviour of $Ce_2Zr_2O_7$. Ignoring these constraints, we further find that a spinon-only fit is unable to account for the dominant quasielastic signal we report.

Magnetic disorder. Considering the importance that disorder can have on the low-energy physics of highly frustrated magnets, one could be concerned that the signal might be due to disorder. However, the quasielastic signal differs significantly from what is expected of conventional magnetic disorder. First, magnetic scattering is expected to have very weak wavevector dependence for an impurity-induced spin-glass state. For example, in classical spin glass such as $Cu_{1-x}Mn_x$ with $x = 0.0165$ and $x = 0.033$, the a.c. susceptibility shows clear hysteresis, and the imaginary part of dynamic susceptibility is weakly **Q** dependent and has a broad peak near 2 meV (ref. 65). This is clearly different from $Ce_2Zr_2O_7$ in which there is no frequency-dependent a.c. susceptibility and the magnetic scattering is momentum dependent. This is especially clear by looking at M_y in Fig. 3 in which we see strong scattering along the First Brillouin zone boundary and a slow decrease in intensity for larger values of h in the $[h, h, 0]$ direction. Next, for magnetic disorder such as in spin glasses where spin directions are randomly frozen in space, one naively expects spin excitations to be isotropic in spin space (that is, $M_y \approx M_z$ for all **Q** values). By contrast, the quasielastic magnetic scattering from $Ce_2Zr_2O_7$ is isotropic at certain points, but anisotropic with $M_y > M_z$ at others. This is clear from Fig. 3a–c. The spin-space anisotropy is also momentum dependent, thereby giving further support to our previous point about the momentum dependence of the quasielastic signal. For these reasons, it is quite challenging to reconcile our measurements with magnetic disorder. By contrast, our modelling in terms of emergent quantum electrodynamics captures the observed momentum and polarization dependencies. It is also hard to reconcile how the disorder could be significant enough to lead to a dominant quasielastic signal and not significantly affect the multiple inelastic spinon peaks, or the cubic scaling of the low-temperature heat capacity.

Fits and comparison between theoretical predictions and experiments

When comparing experimental and theoretical results, the theoretical prediction is convolved with a Gaussian distribution to consider finite experimental resolution. For example, when computing the theoretical predictions for the momentum scans at the elastic position $E = 0$ meV and $E = 0.1$ meV, the theoretical predictions are convolved with a Gaussian with the same FWHM as the experimental resolution. We also fix the global prefactor C introduced in equation (19) to the one that yields the best agreement with experiments. C is chosen consistently between the theoretical calculations reported in Figs. 2–4.

To obtain the optimal parameter sets, we minimize the goodness-of-fit measure as $\chi^2 = \sum_E (I_{E,Q}^{\text{Theory}} - I_{E,Q}^{\text{Experiment}})^2/\Delta I_{E,Q}^{\text{Experiment}}$ where $I_{E,Q}^{\text{Experiment}}$ is the intensity of the signal (that is, $M_z + M_y$ and $M_z - M_y$) measured experimentally at energy E for the energy scans at the three different momentum points Q presented in Fig. 2 and $\Delta I_{E,Q}^{\text{Experiment}}$ is the associated uncertainty. For this fit, we do not fix the width of that Gaussian we convolve the results with, but use it as a free parameter to be optimized. We allow the FWHM of this broadening function to be within 50% of the experimental resolution. Such a fitting procedure yields $\mathcal{J}_x = 0.076$ meV and $\mathcal{J}_\pm = 0.021$ meV. These parameters are approximately 1.2 times the ones in ref. 42 (that is, the ratio $\mathcal{J}_\pm/\mathcal{J}_x$ is the same). We find that the goodness of fit is very shallow as a function of c_{QSI}. An extended range of values of c_{QSI} and θ yields very reasonable and similar fits. In cases where the photon energy for a small c_{QSI} is much smaller than the experimental resolution, the photon signal essentially yields a Gaussian centred at the elastic position after the convolution procedure outlined above. Therefore, c_{QSI} and θ cannot be uniquely determined with the energy scans of Fig. 2. We find acceptable agreement for $\hbar_{c\text{QSI}}/a_0 \in [0.0004, 0.0028]$ meV. The lower bound on the speed of emergent light is introduced since, for lower values, the dynamics of the two-in–two-out manifold should be completely classical. For every speed of light in this interval, we determine an optimal θ by requiring that the ratio of the spinon and photon signals remains consistent. These optimal values of θ are in the range $[0.05\pi, 0.12\pi]$.

To determine the optimal speed of light within the above parameter range, we fit the elastic scans of M_y and M_z presented in Fig. 3 using a similarly defined goodness of fit as $\chi^2 = \sum_Q (I_{E=0,Q}^{\text{Theory}} - I_{E=0,Q}^{\text{Experiment}})^2/\Delta I_{E=0,Q}^{\text{Experiment}}$, where $I_{E=0,Q}^{\text{Experiment}}$ is now the intensity of the elastic signal (that is, M_y and M_z at $E = 0 \pm 0.03$ meV) measured experimentally at the momentum transfer Q. The optimal speed of light saturates the upper bound defined from fitting the energy scans of Fig. 2 such that $\hbar_{c\text{QSI}}/a_0 = 0.0028$ meV. If we do not impose the above upper bound on c_{QSI}, we find that the goodness of fit for the elastic scan monotonically decreases with the speed of light up to about $\hbar_{c\text{QSI}}/a_0 \approx 0.003$ meV. In summary, the optimal speed of light consistent with the energy scans presented in Fig. 2 and the elastic momentum scans of Fig. 3 is 0.0028 meV. The corresponding value of the angle is $\theta = 0.12\pi$.

Of all the parameters we estimate, θ is the most uncertain since it relies on a quantitative comparison between the dynamical spin structure factor obtained by GMFT and Gaussian quantum electrodynamics. It remains unclear to what extent this quantitative comparison between the two is accurate. The main point of the theoretical fit is not to offer a quantitative estimate of θ, but rather to reproduce the experimental results using a small value of θ as well as $\mathcal{J}_x$ and $\mathcal{J}_\pm$ that are reasonably consistent with previous work[42,49]. Furthermore, it should be mentioned that previous QMC investigations on 0-flux QSI at small (that is, $T < 12\mathcal{J}_\pm^3/\mathcal{J}_\parallel^2$) and intermediate (that is, $12\mathcal{J}_\pm^3/\mathcal{J}_\parallel^2 < T < \mathcal{J}_\parallel/2$) temperatures found that the photon contribution to the dynamical spin structure factor is about one to four orders of magnitude larger than the inelastic spinon contribution[28]. Such intensity ratios between the spinon and photon contributions are consistent with our modelling. The estimated θ should, thus, be of the right order of magnitude.

Specific heat measurements and data evaluation

Specific heat measurements were performed in a cryogen-free dilution refrigerator (CF-CS110-1000M-2PT) from Leiden Cryogenics using relaxation calorimetry. The setup is shown in Extended Data Fig. 9a. It consists of a Ag frame and a Ag sample stage suspended by

superconducting NbTi wires, which also serve as electrical leads to the thermometer and heater, thermally insulating them from the bath. All electrical connections to the frame were made via two-component Ag epoxy (Polytec EC101). The thermal link to the bath is provided via a 50-μm Au wire that is spot-welded to the sample platform and glued with Ag paint (DuPont 4929N) to the frame. The thermometer and heater are 1.58-kΩ and 1-kΩ RuO_2 chip resistors, respectively. To improve thermalization, the tin substrate of the thermometer chip was removed with hydrochloric acid and the bare RuO_2 film was then glued on sheets of 25-μm Ag foil using Ag epoxy to increase the thermal contact area. The heater chip was prepared in a similar way with the exception that a prior removal of the Au substrate was not necessary in this case. Both chips were contacted with NbTi wires that were spot-welded to the respective Ag foils and subsequently secured with Ag epoxy. These devices were then glued to the back of the sample stage using GE varnish with a thin insulating layer of cigarette paper in between (Extended Data Fig. 9a,b). Both were calibrated against the mixing-chamber thermometer before the measurements. To improve the reproducibility of calibration, the chip resistors were first thermally cycled several tens of times between room temperature and liquid-nitrogen temperatures.

The resistance of the thermometers was measured using a Lakeshore LS370 resistance bridge with an excitation current between 3.16 nA and 10 nA depending on the temperature. The current for the heater was generated by a Yokagawa GS200 d.c. current source and the applied heating power was monitored by measuring the preamplified (NF Corporation SA-410F3 low-noise differential amplifier) heater voltage with a PicoScope 5000 Series USB oscilloscope.

A sample from the same batch as that used in the neutron scattering investigation was polished to a platelet with a thickness of about 180 μm and a mass of (3.3 ± 0.1) mg using 2,400-grit and 4,000-grit sand paper and a lapping tool. The sample was mounted on the platform with a small amount of Ag paint, which is expected to have a negligibly small addenda contribution.

The addenda of the empty platform were determined before the actual measurements and amount to between 0.14 μJ K^{-1} and 0.43 μJ K^{-1} in the relevant temperature range. The addenda contribution to the total heat capacity with the mounted sample was at a maximum of 44% at the lowest temperature and less than 6% at 100 mK. The addenda as measured before the sample measurement and the ones determined in the fits described below have very similar temperature dependencies.

The data obtained with the sample mounted were evaluated using the relaxation method, as described elsewhere[66]. The total heat capacity, the addenda heat capacity and the relevant thermal links were determined by fitting the relaxation curves on heating the sample ($t_{on} \le t \le t_{off}$, where t_{on} and t_{off} are the time at which the constant heating power was turned on and off, respectively) with a double-exponential decay. This two-tau model is required due to the finite thermal conductance between the sample and the addenda, as well as the expected low thermal conductivity of the sample itself. The error in our specific heat data is estimated to be at a maximum of 10% at 100 mK and up to 20% at the lowest temperatures. We also estimate a maximum error in the temperature of the sample, which amounts to 10% on average (depending on whether a larger or smaller heater power was used). The error bars are shown in the figures discussed below.

The data compare well with the published results (Extended Data Fig. 9d,e), particularly for measurements on single crystals[39,42]. The data in ref. 67 were measured on a powder and show somewhat larger deviations, as expected. As usual, scaled temperature dependencies show higher reproducibility between measurements done with different setups than absolute values. Deviations in the latter can arise from uncertainties in the determination of the sample mass, small sample composition differences between samples of different groups or batches, surface or oxidation effects, and minor systematic errors associated with the different setups and evaluation methods. To limit the effect of these absolute value errors, we took the average of the two previous single-crystal datasets[39,42], both measured using commercial devices, at a 'standard' temperature of 100 mK (Extended Data Fig. 9b, star), and scale all the datasets to this value at 100 mK. We assume that this produces the most accurate absolute values. The scaling factor is 1.125 for our measurements, 1.025 for the data from ref. 39 and 0.965 for the data from ref. 42. This plot shows that in the overlapping temperature range, the temperature dependence of our data is in excellent agreement with the ones on single crystals determined previously[39,42]. At higher temperatures, deviations between those two single-crystal measurements reach up to 43%.

At the lowest temperatures, the data are well described by a cubic temperature dependence, as seen by the fit $C = BT^3$ (straight line with a slope of 3 in the double-logarithmic plot), with B = (7,601 ± 397) J mol_{Ce}^{-1} K^{-4}. When fitting the data below 50 mK with an open power, the fit yields the same power of 3 within the error bars (see the 'Quality of fits to the specific heat data' section). This temperature dependence is well known for acoustic phonons in the Debye model. However, phonons can be firmly ruled out as the source of this dependence here, as the following estimates demonstrate. Assuming a Debye temperature of 260 K (ref. 68), we calculate a phonon specific heat of 0.6 mJ mol_{Ce}^{-1} K^{-1} at 100 mK, which is less than 0.1% of our data at this temperature. Inversely, using the slope of the experimentally determined T^3 dependence (Extended Data Fig. 9f) in a Debye model, we obtain a Debye temperature of 1.4 K, which is unphysically small. This is further supported by the measurements of the non-f electron reference material $La_2Zr_2O_7$, the specific heat of which is negligibly small below 10 K (refs. 39,42). As the phonon contribution is negligible in the temperature range of our measurements, there is no need to subtract any phonon contribution and the entire measured specific heat can be identified as the magnetic contribution C_{mag} (Fig. 5). The cubic temperature dependence of the low-temperature specific heat must, thus, have another origin, and we associate it with the 'photons' of the QSI state discussed in the main text. The velocity of the emergent photons is related to the prefactor B via

$$B = (\bar{R}\pi^2)/60\left(\frac{k_B a_0}{\hbar c_{QSI}}\right)^3, \quad (25)$$

where $\bar{R}$ is the universal gas constant, k_B is the Boltzmann constant and a_0 is the lattice parameter (ref. 30 shows the result quoted per mole of the formula unit $R_2M_2O_7$). This results in a velocity of c_{QSI} = 7.9 ± 0.4 m s^{-1} (that is, $\hbar_{cQSI}/a_0$ = 0.0049 ± 0.0002 meV).

We also determine the entropy release as a function of temperature (Extended Data Fig. 9h) by integrating our C_{mag}/T data together with the data from ref. 39, both scaled as described above, and extended at temperatures below the measurement range by the T^3 fit and at temperatures above the measurement range of ref. 39 by the data from ref. 42 scaled to the data from ref. 39. These extensions are done for completeness but have minimal influence. The entropy reaches a value of 0.89$\bar{R}$ln2 near 10 K. Within the error bars of our new measurements (Extended Data Fig. 9d–h) and an estimated error of 7% on the (scaled) data from ref. 39, the full entropy is reached near 10 K. Thus, within the accuracy of all the specific heat measurements available so far, no evidence for a deviation from the full entropy of Rln2 can be claimed.

Quality of fits to the specific heat data

The quality of fits to the specific heat data is evaluated via the chi-square coefficient of the fits to the data below 50 mK, using the method of orthogonal distance regression. The use of orthogonal distance regression is well suited in this case, given the presence of measurement errors in both absolute value of heat capacity and the sample temperature. Although the T^3 behaviour is observed in a somewhat narrow temperature range, the evidence for this dependence is robust because the specific heat changes strongly (by almost two orders of magnitude) in this temperature range and a large number of data points are available.

Assuming a power-law dependence AT^{α}, the exponent α is well defined (Extended Data Fig. 9f). The power that minimizes the deviation is 3.2 ± 0.2 and, thus, $\alpha = 3$ within small error bars. The optimal reduced chi-square coefficient is less than one, indicating an excellent fit quality. In Extended Data Fig. 9f, we also show fits using $\alpha = 2.5$ and $\alpha = 3.5$. Despite the slight departure change in the exponent, substantial deviations from the measured data are noticed, illustrating that $\alpha = 3$ is the best description of the data.

In Extended Data Fig. 9g, we show that the low-temperature data can alternatively be accounted for by thermally activated behaviour, $A\exp(-\Delta/T)$, with a gap $\Delta = (0.100 \pm 0.006)$ K. This yields an optimal reduced chi-square coefficient comparable with that obtained using a power law. From a purely statistical point of view, we, thus, cannot discriminate between the two behaviours.

However, physical arguments can be made in favour of the power-law interpretation, particularly when trying to discriminate between the two competing scenarios: (1) that $Ce_2Zr_2O_7$ is a frustrated magnet dominated by disorder such that the observed low-energy signal is due to disorder or (2) that $Ce_2Zr_2O_7$ realizes QSI with the low-energy signal coming from emergent photons. A thermally activated behaviour is incompatible with both scenarios. A frustrated magnet dominated by disorder should have a low-temperature heat capacity that scales as a power law. For instance, in spin glasses, a linear scaling of the heat capacity $C(T) \propto T$ is theoretically predicted to arise due to tunnelling between pairs of local energy minima, separated by random potential barriers[69]. Experimentally, a power law ($C(T) \propto T^{\alpha}, 1 \leq \alpha \leq 2$) is generally observed in spin glasses and disordered geometrically frustrated magnets[70–72]. In the case of QSI, the low-temperature heat capacity should scale cubically since the gapless photon dominates the signal over the thermally activated contributions from the gapped excitations.

In summary, although direct fits to the data do not allow statistical differentiation between a cubic scaling and a thermally activated behaviour with a small gap of about 0.1 K, the thermally activated behaviour does not appear physically relevant because neither of the two competing interpretations of the neutron data discussed in this work can be reconciled with such a behaviour (of course, we cannot rule out that other—yet unknown—mechanisms would yield an exponential behaviour). Furthermore, a spin gap of 0.1 K (about 0.009 meV) is not compatible with the observed magnetic excitation spectra of Fig. 2n. Despite the relatively narrow temperature range, we can, therefore, conclude, with good confidence, that a cubic scaling behaviour is the accurate description of the low-temperature specific heat data.

Data availability

The data presented in the article are available from the corresponding authors upon request.

References

64. Wen, J. J. et al. Disordered route to the Coulomb quantum spin liquid: random transverse fields on spin ice in $Pr_2Zr_2O_7$. *Phys. Rev. Lett.* **118**, 107206 (2017).
65. Kofu, M. et al. Magnetic boson peak in classical spin glasses. *Phys. Rev. Res.* **6**, 013006 (2024).
66. Matsumoto, Y. & Nakatsuji, S. Relaxation calorimetry at very low temperatures for systems with internal relaxation. *Rev. Sci. Instrum.* **89**, 033908 (2018).
67. Popa, K. et al. A re-evaluation of the heat capacity of cerium zirconate $Ce_2Zr_2O_7$. *J. Phys. Chem. Solids* **69**, 70–75 (2008).
68. Lan, G., Ouyang, B. & Song, J. The role of low-lying optical phonons in lattice thermal conductance of rare-earth pyrochlores: a first-principle study. *Acta Mater.* **91**, 304–317 (2015).
69. Anderson, P. W., Halperin, B. I. & Varma, C. M. Anomalous low-temperature thermal properties of glasses and spin glasses. *Philos. Mag.-J. Theor. Exp. Appl. Phys.* **25**, 1–9 (1972).
70. Binder, K. & Young, A. P. Spin glasses: experimental facts, theoretical concepts, and open questions. *Rev. Mod. Phys.* **58**, 801–976 (1986).
71. Ramirez, A. P., Espinosa, G. P. & Cooper, A. S. Strong frustration and dilution-enhanced order in a quasi-2D spin glass. *Phys. Rev. Lett.* **64**, 2070–2073 (1990).
72. Nakatsuji, S. et al. Spin disorder on a triangular lattice. *Science* **309**, 1697–1700 (2005).

Acknowledgements

We thank H. Yan, A. Nevidomskyy, A. Scheie, P. Laurell and M. Gingras for helpful discussions and M. Taupin for initial support in setting up the specific heat measurements. The neutron scattering work at Rice is supported by the United States Department of Energy, Basic Energy Sciences, DE-SC0012311 (P.D.). The single-crystal growth work at Rice is supported by the Robert A. Welch Foundation under grant no. C-1839 (P.D.). Crystal growth by B.G. and S.-W.C. at Rutgers was supported by the visitor program at the Center for Quantum Materials Synthesis (cQMS), funded by the Gordon and Betty Moore Foundation's EPiQS initiative through grant no. GBMF6402 and by Rutgers University. F.D. and Y.B.K. are supported by the Natural Science and Engineering Research Council of Canada and the Center for Quantum Materials at the University of Toronto. F.D. is further supported by the Vanier Canada Graduate Scholarship (CGV—186886). D.W.T. acknowledges funding from the European Union's Horizon 2020 research and innovation programme under the Marie Skłodowska-Curie grant agreement no. 884104 (PSI-FELLOW-III-3i). Neutron data (https://doi.org/10.5291/ILL-DATA.4-05-851; https://doi.org/10.5291/ILL-DATA.4-05-904) were obtained using OrientExpress and ThALES instruments at the Institut Laue Langevin with support from proposal nos 4-05-851 and 4-05-904. The specific heat measurements and analyses in Vienna were supported by the European Research Council (ERC Advanced Grant 101055088—CorMeTop) and the Austrian Science Fund (FWF project nos I 5868-N, F 86 and 10.55776/COE1).

Author contributions

P.D. and B.G. conceived of the project. B.G. and S.-W.C. prepared the samples. The neutron scattering experiments were carried out and analysed by D.W.T., P.S., A.H., Y.S., B.G. and P.D. The specific heat measurements were performed by D.M.K., D.H.N. and S.P. Theoretical analysis was supervised by Y.B.K. and performed by F.D. and Y.B.K. The entire project was supervised by P.D. The paper is written by P.D., Y.B.K., B.G. and F.D., with contributions from D.M.K. and S.P. All authors made comments.

Competing interests

The authors declare no competing interests.

Additional information

Extended data is available for this paper at https://doi.org/10.1038/s41567-025-02922-9.

Supplementary information The online version contains supplementary material available at https://doi.org/10.1038/s41567-025-02922-9.

Correspondence and requests for materials should be addressed to Silke Paschen, Yong Baek Kim or Pengcheng Dai.

Peer review information *Nature Physics* thanks the anonymous reviewers for their contribution to the peer review of this work.

https://doi.org/10.1038/s41567-025-02922-9

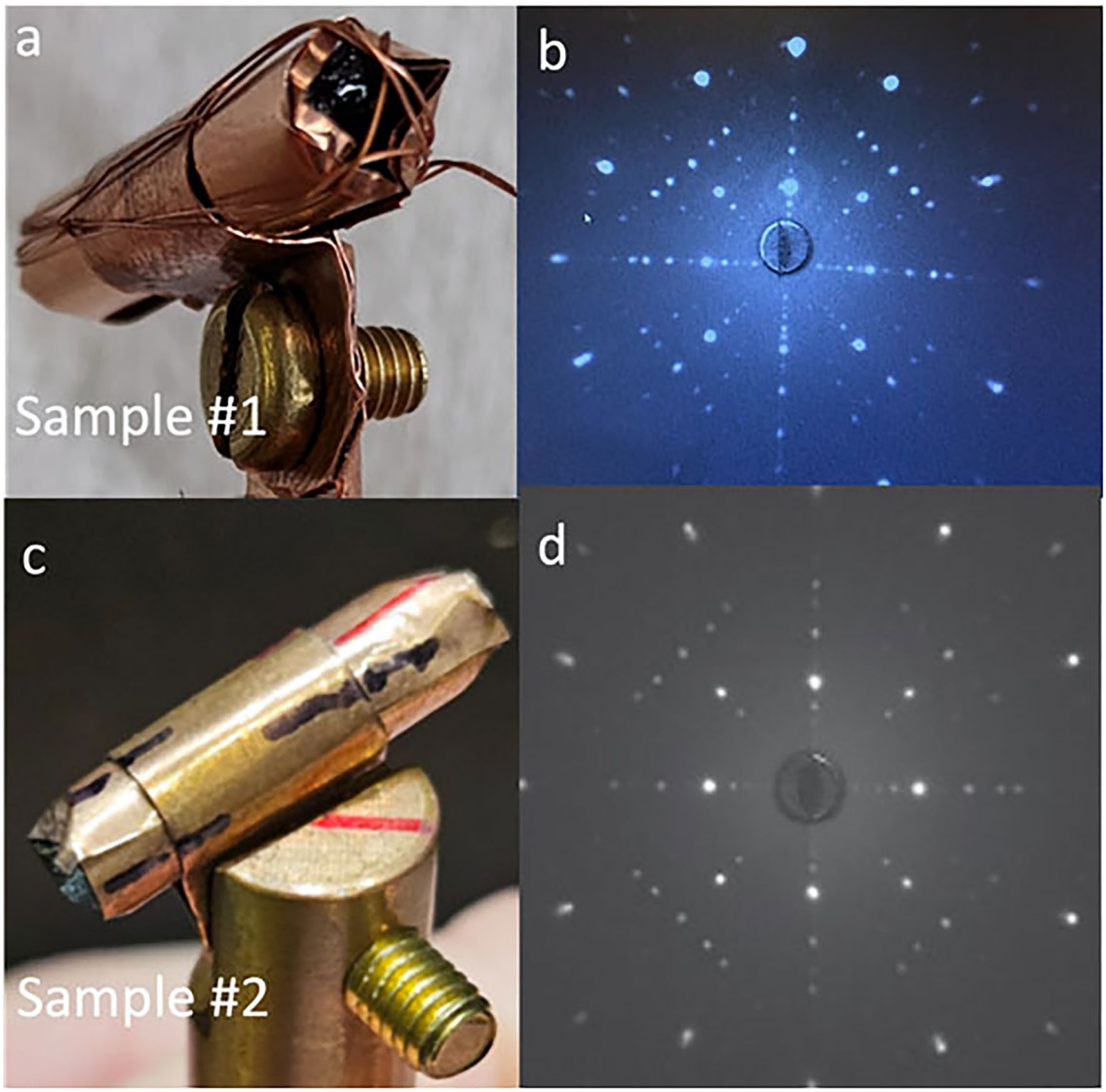

Extended Data Fig. 1 | Pictures of samples. a, One piece of single-crystalline $Ce_2Zr_2O_7$ was mounted on a copper holder. **b**, The X-ray Laue pattern in the [0, 0, 1] direction. The sample is mounted inside a dilution refrigerator maintained at $T = 50$ mK for the entire experiment. The sample is tied inside copper foils to ensure good thermalization at 50 mK (sample 1). **c**, **d** show pictures of sample 2 and its Laue pattern, respectively.

https://doi.org/10.1038/s41567-025-02922-9

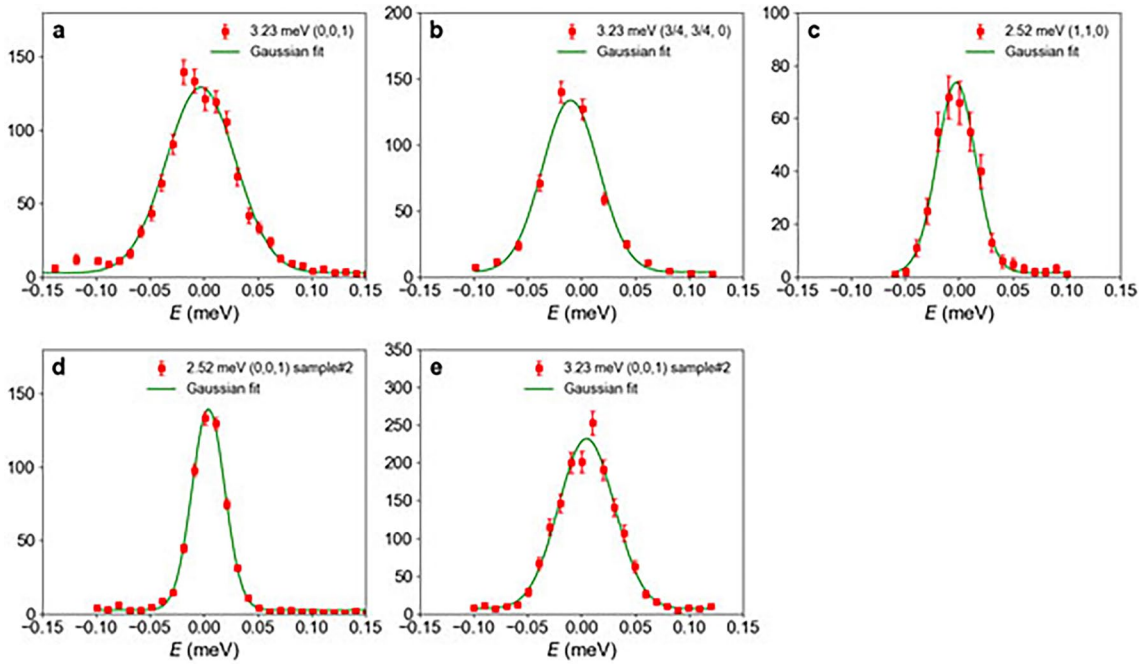

Extended Data Fig. 2 | Raw data of energy scans. a-c, The energy scan of $\sigma_x^{NSF}(\boldsymbol{Q}, E)$ channel at $\boldsymbol{Q} = (0, 0, 1)$, $(3/4, 3/4, 0)$ and $(1, 1, 0)$ using $E_f = 3.23, 3.23,$ and 2.52 meV, respectively, measured on sample 1. We use the Gaussian fit to determine the energy resolution to be 0.076 meV, 0.062 meV, and 0.042 meV in FWHM, respectively. **d**, The energy scan of $\sigma_x^{NSF}(\boldsymbol{Q}, E)$ channel at $\boldsymbol{Q} = (0, 0, 1)$ using $E_f = 2.52$ meV on sample 2, which has an energy resolution of 0.035 meV in FWHM. The curve is shown as the solid black line in Fig. 2n. **e**, Similar energy scan using $E_f = 3.23$ meV on sample 2, which gives an energy resolution of 0.052 meV in FWHM. The vertical error bars in **a**–**e** are statistical errors of 1 standard deviation.

https://doi.org/10.1038/s41567-025-02922-9

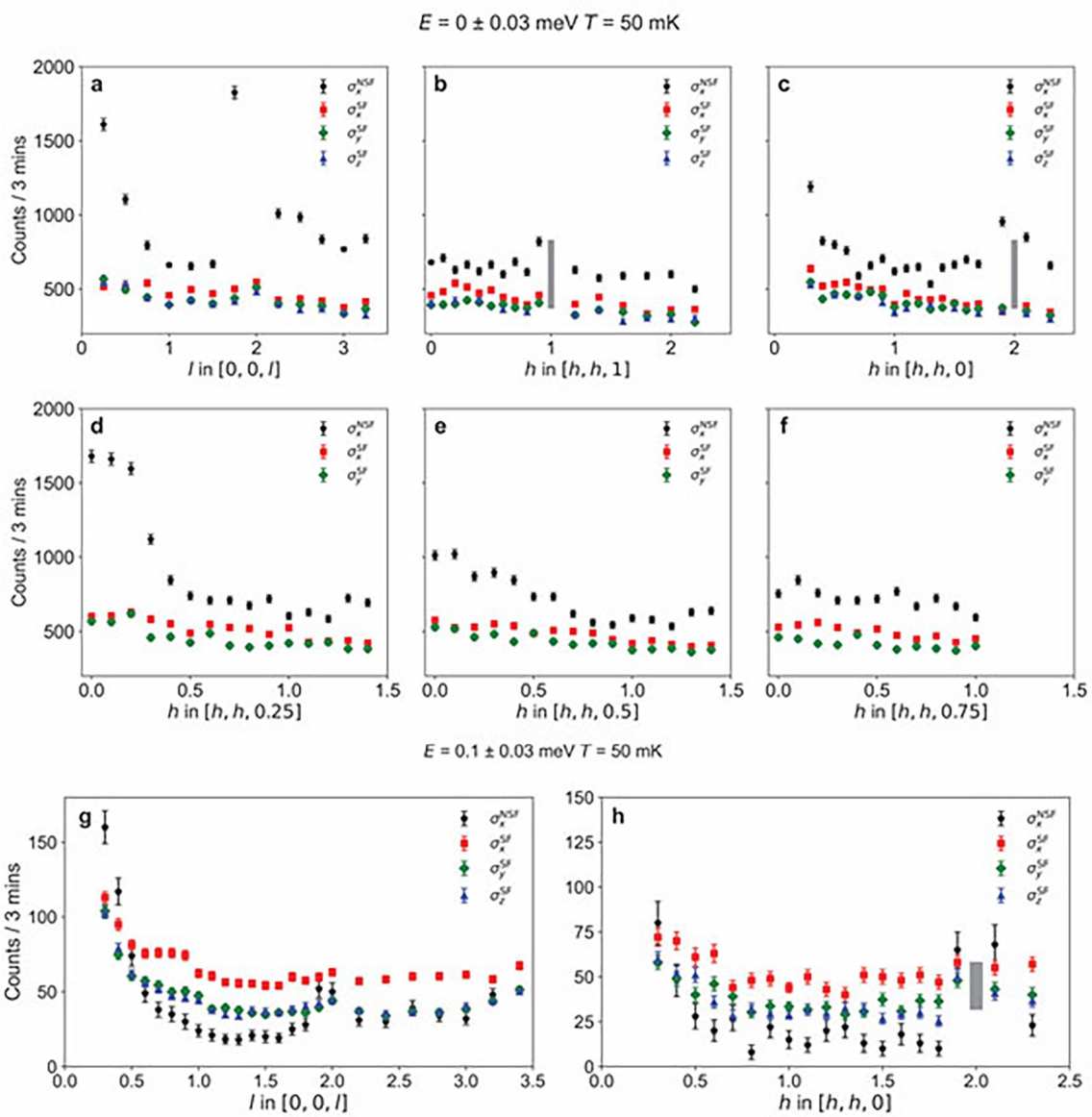

Extended Data Fig. 3 | Raw data of energy scans. a-f, Comparison of the polarized NSF neutron scattering cross sections $\sigma_x^{NSF}(\boldsymbol{Q}, E)$ and SF neutron scattering cross sections $\sigma_{x,y,z}^{SF}(\boldsymbol{Q}, E)$ (**a-c**) and $\sigma_{x,y}^{SF}(\boldsymbol{Q}, E)$ (**d-f**) at $E = 0 \pm 0.03$ meV along the [0, 0, *l*], [*h*, *h*, 1], [*h*, *h*, 0], [*h*, *h*, 0.25], [*h*, *h*, 0.5] and [*h*, *h*, 0.75] directions. $\sigma_x^{NSF}(\boldsymbol{Q}, E) > \sigma_{x,y,z}^{SF}(\boldsymbol{Q}, E)$ at all $\boldsymbol{Q}$ points in the scattering plane. **g**-**h**, Comparison of the polarized $\sigma_x^{NSF}(\boldsymbol{Q}, E)$ and $\sigma_{x,y,z}^{SF}(\boldsymbol{Q}, E)$ at $E = 0.1 \pm 0.03$ meV along the [0, 0, *l*] and [*h*, *h*, 0] directions. $\sigma_x^{NSF}(\boldsymbol{Q}, E) < \sigma_{x,y,z}^{SF}(\boldsymbol{Q}, E)$ at most $\boldsymbol{Q}$ points in the scattering plane. Gray windows in panels **b, c & h** indicate nuclear Bragg peaks at (1, 1, 1) and (2, 2, 0) points, respectively. Data are obtained with $E_f = 3.23$ meV. The vertical error bars in **a**–**h** are statistical errors of 1 standard deviation.

https://doi.org/10.1038/s41567-025-02922-9

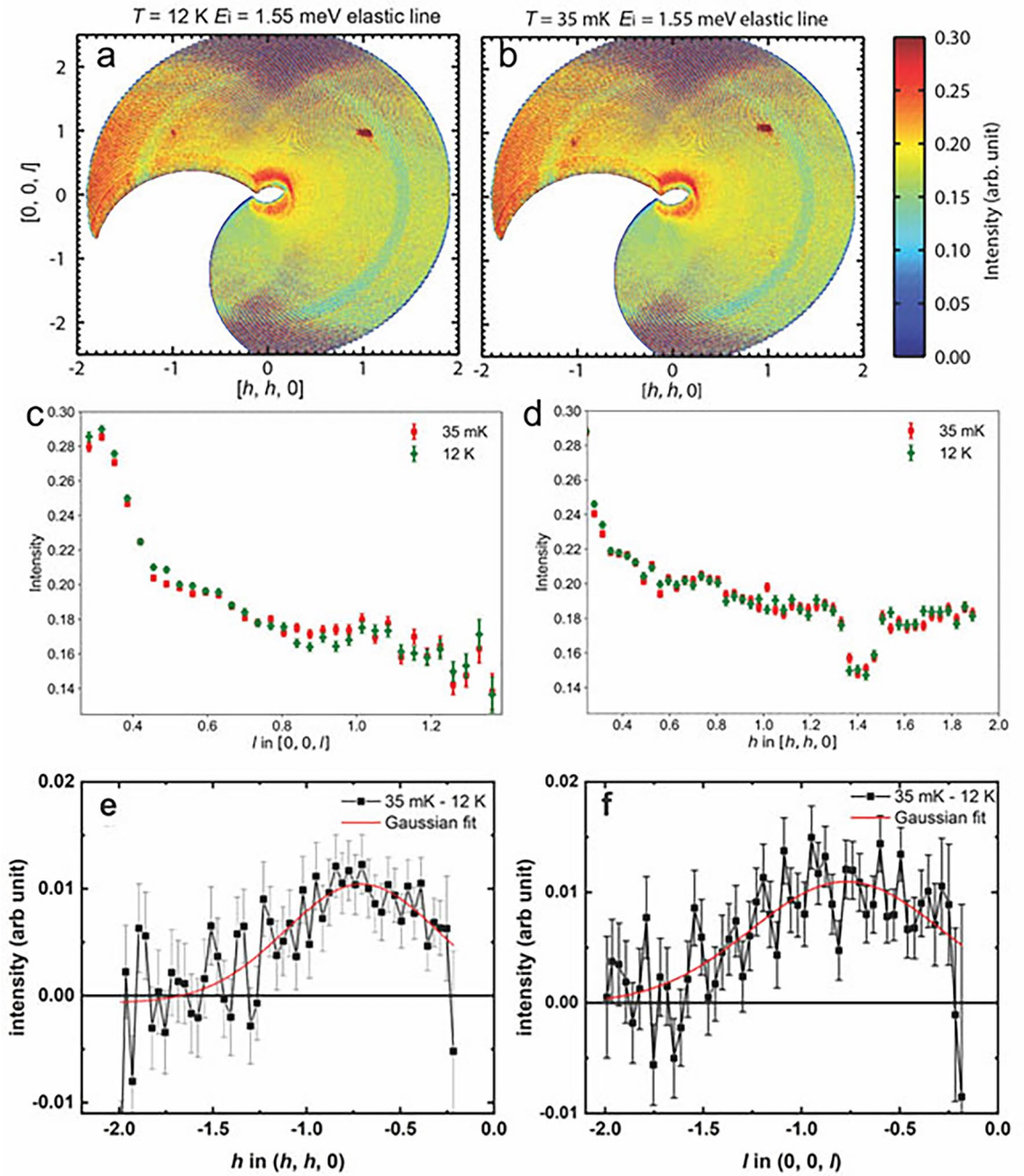

Extended Data Fig. 4 | Unpolarized neutron scattering data. a,**b**, The raw scattering intensity at 35 mK and 12 K using E_i = 1.55 meV at the elastic line (E = 0 ± 0.03 meV) from our previous unpolarized neutron scattering experiment at CNCS[17]. **c**,**d**, The comparison of raw scattering intensity at 35 mK and 12 K along the [0, 0, *l*] and [h, h, 0] directions from cuts using panel **a**. As one can see, the scattering is highly structured and the scattering has higher intensity at 12 K at almost all ***Q*** space probed. **e**,**f**, Inelastic scattering signals obtained at 35 mK by subtracting 12 K as background along the (*h*, *h*, 0) and (0, 0, *l*) directions from our previous unpolarized INS experiment at CNCS[17] and the corresponding Gaussian fits. The vertical error bars in **c**-**f** are statistical errors of 1 standard deviation.

https://doi.org/10.1038/s41567-025-02922-9

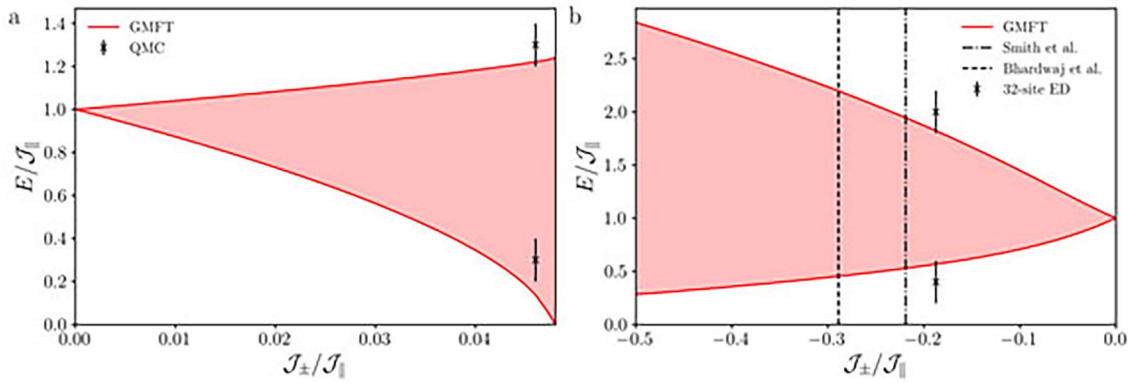

Extended Data Fig. 5 | Theoretical calculations. Predictions from GMFT for the width of the two-spinon continuum as a function of transverse coupling for **a**, 0-flux QSI and **b**, π-flux QSI. We compare these with QMC results of Ref. 47 and the 32-site ED results of Ref. 29 extracted from the transverse dynamical spin structure factor $S^{\pm}(\boldsymbol{Q}, E)$ for 0- and π-flux QSI, respectively. The dashed and dashed-dotted lines denote the parameter sets obtained in Refs. 28,20.

https://doi.org/10.1038/s41567-025-02922-9

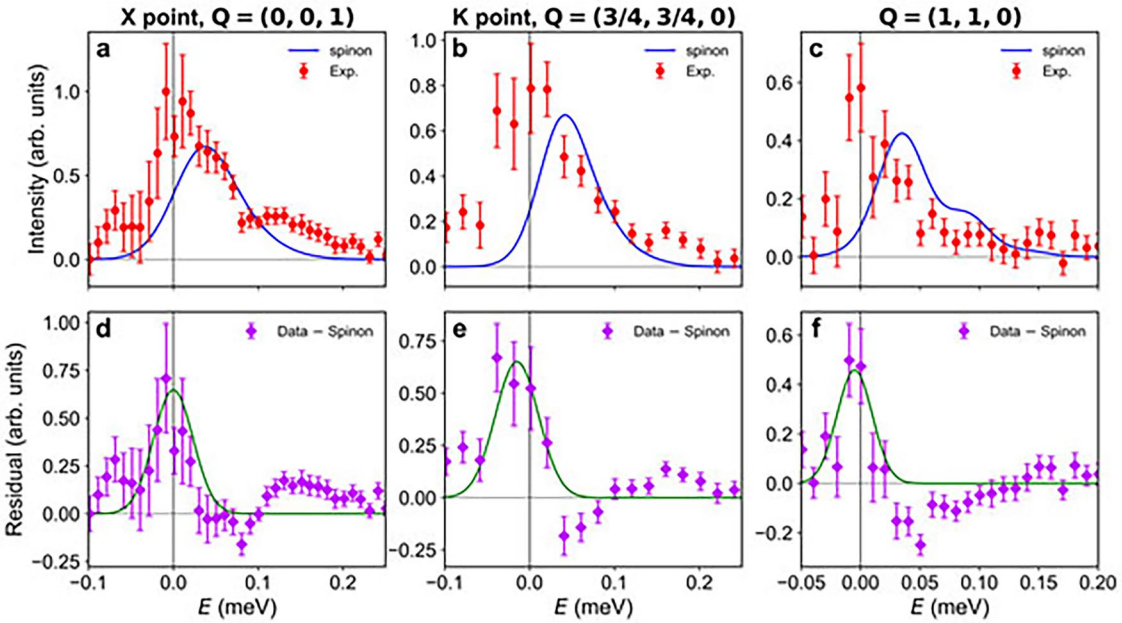

Extended Data Fig. 6 | Comparison of theory and data. a-c, Total magnetic scattering $M_z + M_y$ as a function of energy and theoretical prediction for the spinon contribution using $\mathcal{J}_{\parallel} = 0.06$ meV and $\mathcal{J}_{\pm}/\mathcal{J}_{\parallel} = -0.35$ at $\boldsymbol{Q} = (0, 0, 1)$ (X point), $\boldsymbol{Q} = (3/4, 3/4, 0)$ (K point), and $\boldsymbol{Q} = (1, 1, 0)$. The theoretical results are broadened using a Gaussian with a FWHM of 0.076 meV, 0.062 meV, and 0.042 meV at the X, K and $\boldsymbol{Q} = (1, 1, 0)$ point, respectively. **d-f**, Residual of the fit using only the spinons. The residual is fitted at all three momentum transfers using a Gaussian function centered close to the elastic line. The vertical error bars are propagating errors using Eq. (3).

https://doi.org/10.1038/s41567-025-02922-9

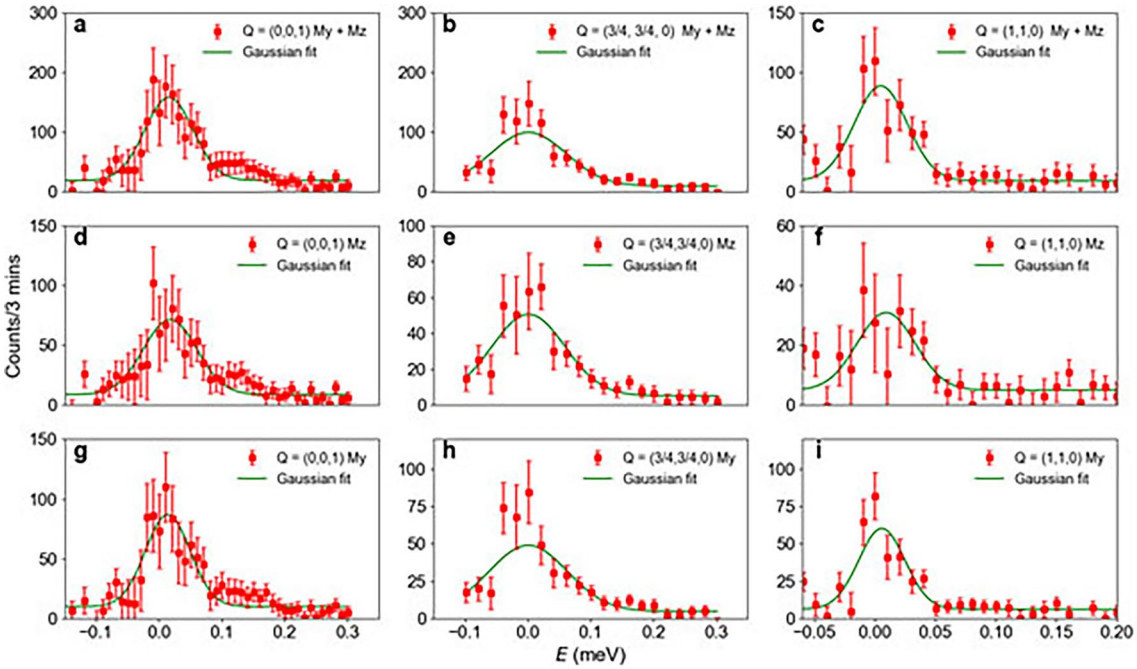

Extended Data Fig. 7 | Comparison of theory and data. a-i, The energy scan of pure magnetic components $M_z + M_y$, M_z, and M_y at $\boldsymbol{Q} = (0, 0, 1)$, $(3/4, 3/4, 0)$ and $(1, 1, 0)$. We use the Gaussian fit to determine the relative shift of the signals compared with the elastic line. The vertical error bars are propagating errors using Eq. (3).

https://doi.org/10.1038/s41567-025-02922-9

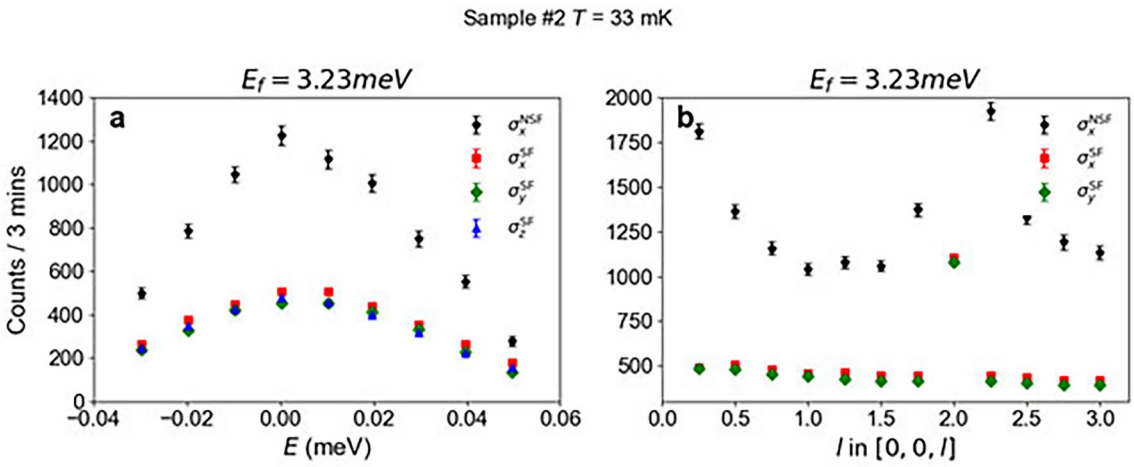

Extended Data Fig. 8 | Raw data of high resolution measurements. a, The raw energy scan around the elastic line of the second sample at $\boldsymbol{Q} = (0, 0, 1)$ using the same setup as the first sample, $E_f = 3.23$ meV. **b**, The raw data of the polarized $\sigma_x^{NSF}(\boldsymbol{Q}, E)$ and $\sigma_{x,y}^{SF}(\boldsymbol{Q}, E)$ at $E = 0 \pm 0.02$ meV using $E_f = 3.23$ meV along the $[0, 0, l]$ direction. The vertical error bars represent statistical errors of 1 standard deviation.

https://doi.org/10.1038/s41567-025-02922-9

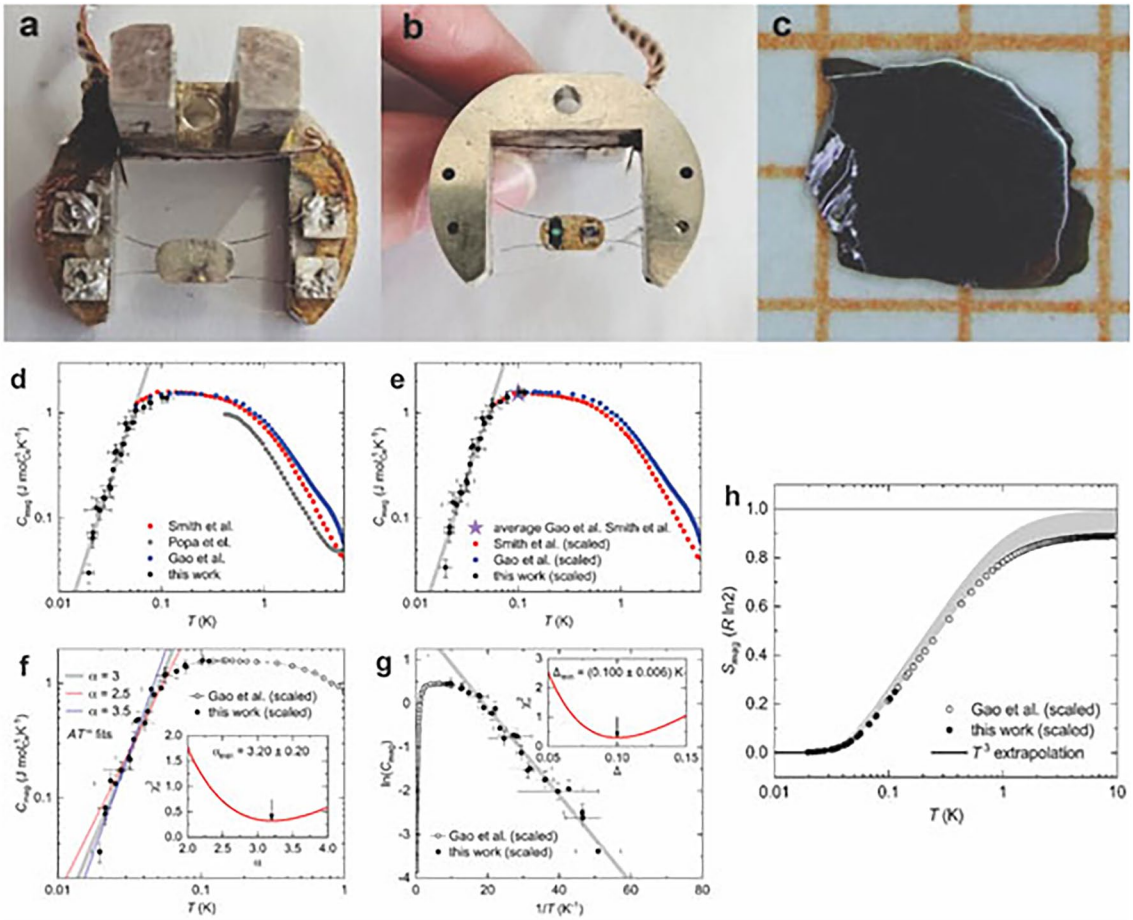

Extended Data Fig. 9 | Summary of heat capacity measurements. a Top view of the sample holder for specific heat measurements, showing the silver sample stage suspended by NbTi wires from the silver frame that was directly screwed to the mixing chamber of the cryostat, as well as the gold wire serving as thermal link to the bath. **b** Bottom view of the sample holder showing the thermometer (left) and heater (right) chips that are glued to the sample stage with GE varnish. **c** Single-crystalline sample of $Ce_2Zr_2O_7$ used for specific heat measurements. **d** Comparison of the specific heat data of $Ce_2Zr_2O_7$ obtained in this work with published results[39,42,67]. The grey line is a guide to the eyes. **e** Same data as in **a**, except for the data measured on powder down to only 0.4 K[67], rescaled to the average of the data points of Smith et al.[42] and Gao et al.[39] at 100 mK, which is deemed to be the most precise estimate of the absolute magnitude of the specific heat of $Ce_2Zr_2O_7$ at this temperature. The grey line is a cubic-in-temperature fit to data below 50 mK. **f** Magnetic specific heat data on $Ce_2Zr_2O_7$ as a function of temperature on double-logarithmic scales, compared to power-law fits, AT^{α}, with fixed powers α of 3 (grey), and 2.5 (red) and 3.5 (blue) for comparison, illustrating that $\alpha = 3$ describes the data best. A minimization procedure with open α yields the $\chi^2_v(\alpha)$ dependence shown in the inset, confirming that, within the error bars, $\alpha = 3$ is the best description of the data. **g** Arrhenius plot of the magnetic specific heat together with a linear fit to the data (grey line), showing that the low-temperature specific heat of $Ce_2Zr_2O_7$ could also be accounted for by a thermally activated behavior, with a gap of 0.1 K (inset). Both fits yield similar minimal χ^2_v, preventing discrimination between the two on purely statistical grounds. **h** Magnetic entropy release as function of temperature obtained by integrating our C_{mag}/T data (full black symbols) together with previously published C_{mag}/T data[39] (open symbols), both scaled as done in **e**. Within the error of the measurements, the full entropy of $R\ln 2$ is reached at 10 K (grey shaded area). The vertical error bars in **d**-**g** are estimated to be at a maximum 10 % at 100 mK and up to 20 % at the lowest temperatures. Horizontal error bars represent maximal errors in the temperatures of the sample, which amount to 10 % on average (depending on whether a larger or smaller heater power was used).